

Department of Physics
Faculty of Science
University of Helsinki

LENGTH CALIBRATION OF FOURIER DOMAIN INTERFEROMETER FOR PARTICLE ACCELERATOR QUALITY ASSURANCE

Risto Montonen

ACADEMIC DISSERTATION

To be presented, with the permission of the Faculty of Science
of the University of Helsinki, for public examination in Auditorium XIV
of the University of Helsinki main building, Unioninkatu 34,
on August 24th 2018, at 12 o'clock noon.

Helsinki 2018

Supervisors

Prof. Edward Hæggström
Doc. Ivan Kassamakov
Prof. Kenneth Österberg

Department of Physics
University of Helsinki
Helsinki, Finland

Reviewers

Prof. Eustace L. Dereniak
The University of Arizona
Tucson, The United States of America

Prof. Malgorzata Kujawska
Warsaw University of Technology
Warsaw, Poland

Opponent

Prof. Wolfgang Osten
University of Stuttgart
Stuttgart, Germany

Cover art: Schematic presentation of optical thickness and group refractive index measurement of a glass transfer standard using a Sagnac type interferometer.

Report Series in Physics HU-P-D259

ISBN 978-951-51-2785-3 (printed version)
ISBN 978-951-51-2786-0 (PDF version <http://ethesis.helsinki.fi>)
ISSN 0356-0961

Unigrafia
Helsinki 2018

ABSTRACT

Following development of the Large Hadron Collider at CERN (European Laboratory for Particle Physics), a viable option for the future frontiers of particle physics would be the Compact Linear Collider (CLIC). For efficient collider operation, the internal alignment and shape of the particle accelerating structures is crucial, as even micrometer-level misalignments reduce the performance of CLIC. Destructive quality assurance methods exist that require cutting the structure into two halves but prevent subsequent use of the accelerating structure.

I propose a fiber-optic Fourier domain short coherence interferometer (FDSCI) for quality assurance of the accelerating structure. The method provides submicron accuracy, 10 mm measurement range, and nondestructive access inside the hard-to-reach accelerator cavity.

The method relies on length calibration that employs transparent plate transfer standards of a certified geometric thickness. FDSCI actually measures the optical thickness, and these two lengths are related to each other through the group refractive index. In this thesis the group refractive index of the transfer standards was quantified using a balanced Sagnac type interferometer. The calibration provided a function that can be used to correct the bias in the measurement system. The concept was validated by measuring a step profile on a copper disc manufactured to the same tolerances that are required from the accelerating structures. Uncertainty analysis, including contributions from the calibration, measurement repeatability, sample orientation, environmental conditions, and thermal expansion, showed that submicron accuracy was achieved at a 95% confidence level.

A fiber-optic probe provided access inside the accelerator cavity. The probe operates in common-path configuration which automatically compensates for the dispersion in the optical system, thus maintaining the achieved accuracy. The required 10 mm measurement range was achieved by employing a tunable Fabry-Perot filter assisted spectral interferogram acquisition technique.

The fiber-optic FDSCI shows promise in quantifying whether the accelerating structures are assembled to the required tolerances.

ACKNOWLEDGEMENTS

The work for this thesis was conducted in the Electronics Research Laboratory, Department of Physics, University of Helsinki, in co-operation with the Helsinki Institute of Physics, responsible for the Finnish research collaboration with the European Laboratory for Particle Physics (CERN). I acknowledge the directors of the Department of Physics, Professors Juhani Keinonen, Hannu Koskinen, and Kai Nordlund, the activity leader of the Compact Linear Collider X-band technologies, Dr. Walter Wuensch, and directors of the Helsinki Institute of Physics, Professors Juha Äystö, Paula Eerola, and Katri Huitu, for providing the facilities for the research.

I acknowledge CERN K-contract under agreement KE-2488 and doctoral programmes Concurrent Mechanical Engineering (CME) and Particle Physics and Universe Sciences (PAPU) for financial support for my research.

I thank Prof. Edward Hæggström for his support for the research and for his supervision during my entire scientific training. All I know from science at the highest standard I have learned from Prof. Hæggström.

Many thanks belong to Professors Malgorzata Kujawska and Eustace L. Dereniak for their effort in pre-examining my thesis. I sincerely thank Prof. Wolfgang Osten for accepting to serve as an opponent for my dissertation.

I am especially grateful to Doc. Ivan Kassamakov for introducing me to the length metrology and to the fascinating world of optics. I thank him for numerous fruitful discussions on light phenomena. I am also grateful for his help in finding the opponent and reviewers for my thesis.

I thank Prof. Kenneth Österberg for providing me the opportunity to carry out research in the exciting realm of particle physics. Thorough expression of uncertainties in this thesis would not have happened without his supervision.

I thank Prof. Peter Lehmann and his group for co-authoring two papers. I am grateful for the helpful comments during our research.

It has been a pleasure to work with all colleagues in the Electronics Research Laboratory, Helsinki Institute of Physics, and CERN. I thank my teammates Mr. Anton Nolvi, Mr. Antti Meriläinen, Mr. Tuomo Ylitalo, and my roommate Dr. Lasse Franti, with you the long days at work felt shorter and enjoyable. I thank Doc. Ari Salmi for supervising my earlier studies in ultrasonics. It has always been easy to ask your advice in any puzzling problem. I also thank Dr. Markus Aicheler for his help to work at CERN.

And finally, I would like to express my deepest gratitude to my family members, my beloved wife Anni, parents Marjukka and Kalevi, sisters Kirsi and Maria, and brothers Markku and Santeri. Thanks to your tireless support and pull back to everyday life after work, this book exists today.

Risto Montonen, July 2018, Helsinki

CONTENTS

Abstract.....	3
Acknowledgements	4
Contents.....	5
Abbreviations	6
1 Introduction.....	8
2 Claim	10
2.1 List of original publications	10
2.2 Author's contribution	11
3 Theory – Short coherence interferometry	12
4 FDSCI setup to characterize CLIC-AS Internal alignment	16
4.1 Spectrometer FDSCI	16
4.2 Fiber-optic FDSCI.....	19
5 Length calibration	24
5.1 Length transfer standard	24
5.2 Refractive index	26
5.3 Cosine error.....	29
5.4 Thermal expansion	31
5.5 Length calibration function of FDSCI	31
6 Results	32
6.1 Group refractive index quantification	32
6.2 Spectrometer FDSCI length calibration	34
6.3 Step height quantification on copper disc	37
6.4 Qualitative AS-disc internal measurement	41
7 Discussion.....	42
7.1 Relevance of the results towards submicron accurate fiber-optic FDSCI.....	42
7.2 CLIC-AS internal alignment measurement strategy	44
8 Conclusions.....	49
References	50

ABBREVIATIONS

AS	Accelerating structure
BS	Beam splitter
C	Optical circulator
CERN	European Laboratory for Particle Physics
CLIC	Compact LInear Collider
CMM	Coordinate measuring machine
FDSCI	Fourier domain short coherence interferometer
FFP	Fiber Fabry-Perot spectral filter
GRIN	Gradient index lens
IFFT	Inverse fast Fourier transform
L	Lens
LED	Light emitting diode
LHC	Large Hadron Collider
M	Mirror
MMF	Multimode fiber
O	Objective
PD	Photodetector
RF	Radio frequency
RAP	Right angle prism
ROI	Region of interest
SEM	Scanning electron microscope
SNR	Signal-to-noise ratio
SMF	Single mode fiber
SOA	Semiconductor optical amplifier
SWLI	Scanning white light interferometry

Symbols

α	Linear coefficient of thermal expansion
a	Calibration coefficient
c_i	Sensitivity coefficient
C	Calibration function
d	Optical distance
D	Geometric distance
e	Measurement bias
E_{rot}	Eccentricity with respect to rotation axis
φ	Phase shift
f	Focal length
f_{NA}	Aperture function
f_{pp}	Water vapor partial pressure
f_{sat}	Water vapor partial pressure of saturated moist air

γ	Angular coordinate
$\Delta\gamma$	Angular difference
h	Optical thickness
H	Geometric thickness
H_{step}	Step height
H_R	Relative humidity
I	Intensity
k	Wavenumber
k_o	Central wavenumber
λ	Wavelength
λ_o	Central wavelength
$\Delta\lambda$	–3 dB bandwidth
$\delta\lambda$	Spectral resolution
l_c	Coherence length
L	Length
ΔL	Length difference
n_g	Group refractive index
n_p	Phase refractive index
ν	Maximum interference visibility
N	Number of repeats
NA	Numerical aperture
p	Atmospheric pressure
r	Optical length
r_{max}	Maximum optical measurement range
r_{corr}	Correlation coefficient
R	Geometric length
Ra	Arithmetic mean roughness
P	Reflectance
s	Sagnac beam path difference
$s(x_i)$	Standard deviation
S	System spectrum
θ	Angular error
θ_{max}	Cone angle of light beam
T	Temperature
ΔT	Temperature difference
$u(x_i)$	Standard uncertainty
$u_c(y)$	Combined standard uncertainty
$u_i(y)$	Uncertainty contribution
$u_k(y)$	Correlated uncertainty contribution
U	Expanded uncertainty
W	Wall thickness
X, Y	Lateral coordinates
Z	Vertical coordinate

1 INTRODUCTION

The Compact Linear Collider (CLIC) is a viable option for the future frontier of elementary particle physics research after CERN's Large Hadron Collider (LHC). The LHC results will need to be complemented by precise experiments. Where LHC collides composite particles called hadrons, CLIC is designed to be a precision instrument that collides elementary particles, electrons, and positrons. Due to their relatively low mass, ring-type accelerators are ruled out because of their high synchrotron radiation losses. This calls for a compact (high accelerating gradient) linear particle accelerator (linac) [1]. CLIC employs two-beam linear accelerator technology to sustain a 100 MV/m accelerating gradient [1]. The acceleration power is extracted from a high-current drive-beam that runs parallel to the main linac. From that beam, the extracted radio frequency (RF) electromagnetic power is guided through RF waveguides into the accelerating structures in the main linac. CLIC features two opposing main linacs to permit the electron and positron beams to collide. The particle interaction takes place in a particle detector between the two main linacs.

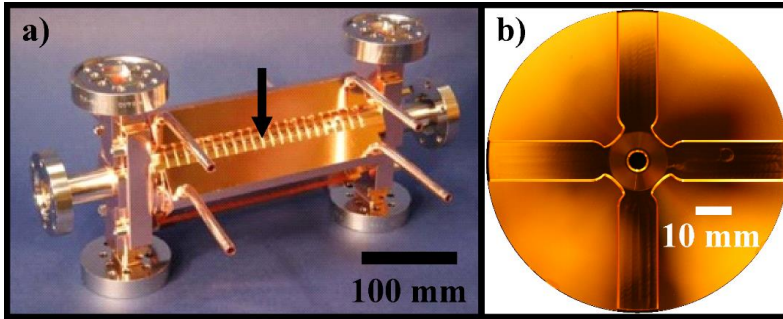


Figure 1 (a) One accelerating structure of the Compact Linear Collider (CLIC) composed of a stack of ultraprecisely machined copper discs. The black arrow indicates the stack of discs. Photograph by Wang *et al.* [2]. (b) One accelerating structure disc with iris in the center.

Accelerating structures are the key components of CLIC. In the 3 TeV and 50 km long CLIC machine, there are over 140,000 accelerating structures [1]. One accelerating structure (AS), Fig. 1(a), is a stack (height 230 mm, diam. 80 mm) of ultraprecisely machined oxygen-free electronic copper discs diffusion bonded together [1, 2]. Each copper disc has a specified internal structure, Fig. 1(b). When stacked together the discs form an RF cavity (AS-cavity). In this cavity the electron/positron beams are accelerated by the RF power. The shape and dimensional tolerances of the AS-cavity are determined by the RF requirements [3]. Even micrometer-level misalignments inside the AS reduce the CLIC performance. Figure 2 depicts

four shape errors in the AS-cavity and their corresponding dimensional tolerances. Tolerance for the AS-cavity diameter is $1\text{ }\mu\text{m}$, whereas tolerance for the iris shape is $2\text{ }\mu\text{m}$, and tolerance for the surface roughness, R_a , is 25 nm [3]. During assembly the discs need to be diffusion bonded with better than $5\text{ }\mu\text{m}$ alignment and less than $140\text{ }\mu\text{rad}$ disc tilt [1].

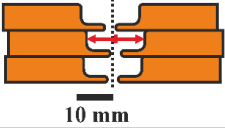
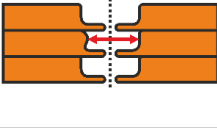
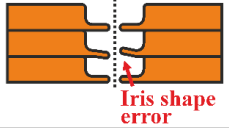

Type 1	Type 2	Type 3	Type 4
Disc stack alignment	AS-cavity diameter	Iris shape	Disc tilt
			
$5\text{ }\mu\text{m}$	$1\text{ }\mu\text{m}$	$2\text{ }\mu\text{m}$	$140\text{ }\mu\text{rad}$

Figure 2 AS-cavity shape errors and their dimensional tolerances.

A contact scanner technique to measure the AS-cavity dimensions exists [4]. This technique cannot ensure the quality of the internal AS-cavity after diffusion bonding of the disc stack without cutting the AS into two halves. After this destructive action, the acceleration performance of the AS can no longer be tested. Therefore, a submicron accurate and nondestructive internal alignment tester that can reach across at least 8.6 mm radius of the AS-cavity is required for AS quality assurance purposes. We propose to quantify the alignment and shape of the hard-to-reach AS-cavity using a fiber-optic Fourier domain short coherence interferometer (FDSCI), Fig. 3. This technique inserts a fiber-optic probe into the AS-cavity without cutting the structure. The internal shape of the AS-cavity is measured point-by-point while retracting the probe and rotating the disc stack.

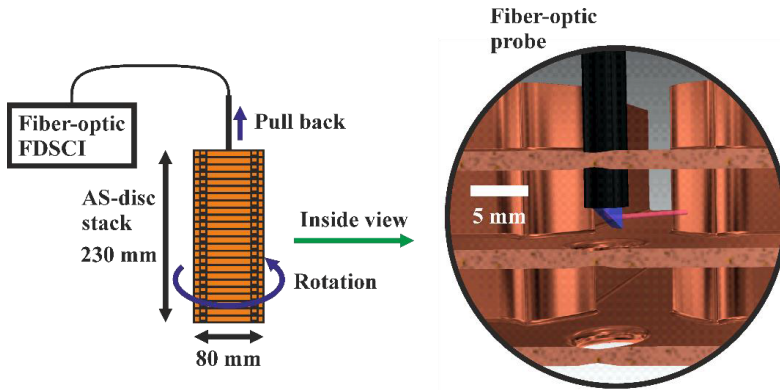


Figure 3 Principle of a fiber-optic Fourier domain short coherence interferometer (FDSCI) employed to quantify the internal alignment of an accelerating structure (AS). Computer-aided design of the AS-discs drawn by Anastasiya Solodko.

2 CLAIM

I claim the ability to calibrate a Fourier domain short coherence interferometer (FDSCI) for the accelerating structure (AS) quality assurance of the Compact Linear Collider (CLIC).

I support my claim by three refereed publications and by one unpublished study. Paper I addressed calibration of an FDSCI setup for absolute length measurements. The setup featured free-space optics and a short measurement range (240 μm). A length calibration scheme based on glass and plastic plate transfer standards was presented, together with accuracy evaluation. In thick plate transfer standards (10 mm), higher order dispersion is significant. Therefore, a group refractive index measurement to relate the specified geometric thickness of plate transfer standards to optical thickness is required. Paper II addressed this problem and provided a group refractive index quantification technique based on a balanced Sagnac type interferometer. Paper III continued the work of paper I towards alignment measurements. Proof of concept was achieved by applying a calibrated FDSCI to quantify a step profile on a copper disc machined to meet the CLIC-AS dimensional tolerances. The unpublished study describes work to develop a fiber-optic FDSCI setup capable of accessing the hard-to-reach AS-cavity. Qualitative results of this study showed feasibility of the fiber-optic probe access and a measurement range exceeding the AS-cavity radius.

2.1 LIST OF ORIGINAL PUBLICATIONS

This thesis summarizes work of three primary publications (I – III).

- I R. Montonen, I. Kassamakov, E. Hæggström, and K. Österberg, “Calibration of Fourier domain short coherence interferometer for absolute distance measurements,” *Applied Optics* **54**(15), 4635–4639 (2015).
- II R. Montonen, I. Kassamakov, P. Lehmann, K. Österberg, and E. Hæggström, “Group refractive index quantification using Fourier domain short coherence Sagnac interferometer,” *Optics Letters* **43**(4), 887–890 (2018).
- III R. Montonen, I. Kassamakov, E. Hæggström, and K. Österberg, “Quantifying height of ultraprecisely machined steps on oxygen-free electronic copper disc using Fourier-domain short coherence interferometry,” *Optical Engineering* **55**(1), 014103 (2016).

Additional original publication by the author

- IV R. Montonen, A. Nolvi, S. Tereschenko, P. Kühnhold, P. Lehmann, E. Hæggström, and I. Kassamakov, “System spectrum conversion from white light interferogram,” *Optics Express* **25**(11), 12090–12099 (2017).

These publications are referred to in the text by their Roman numerals.

2.2 AUTHOR’S CONTRIBUTION

- I RM (R. Montonen) designed the experiments, together with IK (I. Kassamakov), EH (E. Hæggström), and KÖ (Kenneth Österberg). RM constructed the setup, carried out most of the measurements, and did the data analysis. RM wrote the first version of the manuscript, which was then refined by all authors.
- II RM designed the experiments with IK and PL (P. Lehmann), constructed the setup, and carried out all measurements and data analysis. RM wrote the manuscript, which was then refined by all authors.
- III RM designed the experiments with IK, EH, and KÖ, carried out the Fourier domain interferometry measurements, and did the data analysis. RM wrote the manuscript, which was then refined by all authors.
- IV RM designed the experiments with IK, carried out the measurements with AN (A. Nolvi), ST (S. Tereschenko), and PK (P. Kühnhold), and did the data analysis. RM wrote the manuscript, which was then refined together with PL, EH, and IK.

3 THEORY – SHORT COHERENCE INTERFEROMETRY

An interferometer is a tool to measure length using light. In general, interferometry is conducted either in the Fourier domain or in the time domain.

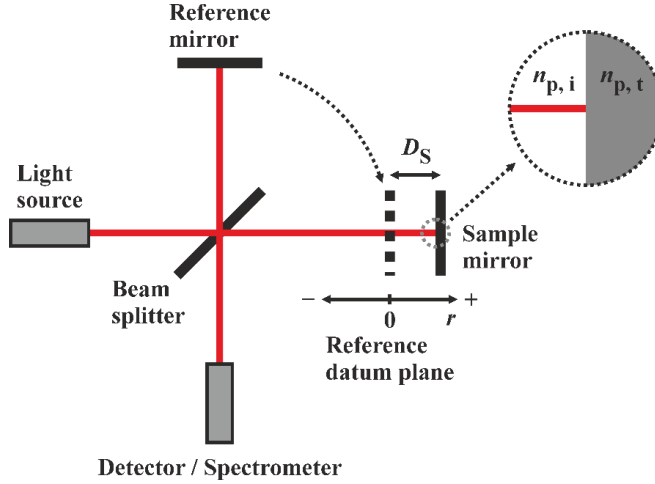


Figure 4 Schematic of an idealized Michelson type interferometer. Abbreviations: r , optical length; D_s , geometric distance; $n_{p,i}$, incident refractive index; $n_{p,t}$, refractive index of the transmitting medium.

A generic Michelson type interferometer is shown in Fig. 4. Parallel light from a light source is split into a reference and a sample path. In Fourier domain interferometry, reflections from a stable reference and a stable sample mirror interfere after the beam splitter and a spectrally resolved interferogram is detected by a spectrometer. Since practical photodetectors measure an electric current photogenerated by kicking a charge carrier over some energy barrier, the detected photocurrent is proportional to the detected light intensity (light power/unit area) [5]. For parallel light, the coherence function that describes the detected light intensity, I , as a function of the wavenumber of light, k , is [6]

$$I(k) = \frac{1}{4}S(k)[P_R(k) + P_S(k)] + \frac{1}{2}S(k)\sqrt{P_R(k)P_S(k)}\cos[-2kn_p(k)D_s], \quad (1)$$

where $S(k)$ is the system spectrum that comprises the light source spectrum and the system transmittance, and $P_R(k)$ and $P_S(k)$ are the reflectances of the reference and the sample mirror. The argument of the cosine function describes the phase difference between the interfering light beams. This

phase difference arises from the optical path length difference between the two interferometer arms, which equals $2n_p(k)D_s$ for the interferometer shown in Fig. 4. Here D_s is the geometric distance between the sample mirror and the reference datum plane, $n_p(k)$ is the phase refractive index of the medium across D_s , and the factor 2 accounts for the round-trip path of the reflected light from the sample mirror. In Eq. (1) the first term represents a path-length independent DC (constant) component, whereas the second term represents interference modulation. The length resolved coherence function, called an A-scan, is found by inverse Fourier transforming $I(k)$:

$$I(r) = |IFT[I(k)]|, \quad (2)$$

where r is the optical length. The magnitude gives the amplitude of the intensity. Usually, only the positive r side of $I(r)$ is plotted. The DC peak is found at zero optical length. As the A-scan represents spatially localized energy that propagates in a medium at group velocity, r is related to the geometric length, R , through the group refractive index, n_g [7]. Therefore, the maximum of the interference peak is at D_s times n_g at the central wavelength of the system, λ_o ; that is, at $r = n_g(\lambda_o)D_s$. In Fourier domain interferometry, this signal measures length. The representation of the r -axis as half the optical path length provides the optical thickness correctly in reflection mode measurements, where the light travels a path length that is twice the optical thickness.

The stationary interferometer arrangement in the Fourier domain allows a semi-transparent reference mirror to be mounted into the sample arm to share the same path as the sample reflection. This common-path configuration cancels dispersion and polarization mismatch in the optical components that are common for the sample and reference light [8]. Avoiding a separate reference path reduces the vibration sensitivity of the interferometer [9]. In contrast to the idealized Michelson type interferometer, Fig. 4, where the sample and reference reflections are external (incident refractive index is less than refractive index of the transmitting medium), one of the reflections in the common-path configuration is internal (incident index is higher than index of the transmitting medium), Fig. 5. This causes a phase shift between the two reflections. The phase shift may be derived from the Fresnel equations [10] using complex refractive indices.

Dispersion due to optical components and phase shifts is taken into account in the coherence function, Eq. (1), as additional terms in the cosine argument [11],

$$-2kn_p(k)D_s + 2(k - k_o)n_{p, \text{comp}}(k)\Delta L_{\text{comp}} + \varphi(k).$$

In the above, the second term describes dispersion due to the optical components, and the third term, $\varphi(k)$, is the phase shift related to the reflection phenomena. k_o is the central wavenumber of the system, $n_{p, \text{comp}}(k)$ is the phase refractive index of the optical components, and ΔL_{comp} is the

length difference of the optical components in the sample and reference path. In common-path configuration the sample and reference light share the same optical components, and therefore $\Delta L_{\text{comp}} = 0$. Hence, dispersion due to the optical components is canceled. In dispersion uncompensated interferometers, where $\Delta L_{\text{comp}} \neq 0$, dispersion due to the optical components affects the measured absolute length, depending on the system spectrum. For clear transparent glass samples, Fig. 5(a), which have a negligible extinction coefficient at visible and near infrared wavelengths, the phase shift term is π . This wavenumber invariant phase shift does not affect the form of $I(r)$ because of the magnitude operation, Eq. (2), and hence does not affect the measured absolute length. In copper measurement, Fig. 5(b), the extinction coefficient of copper is nonzero and depends on the wavenumber. This causes a wavenumber dependent phase shift, which affects the measured absolute length. For copper, this measurement error is less than 60 nm with the light sources used in this thesis. However, this measurement error is equal everywhere on a copper sample, and therefore, it does not affect differential measures, as would a step height measurement.

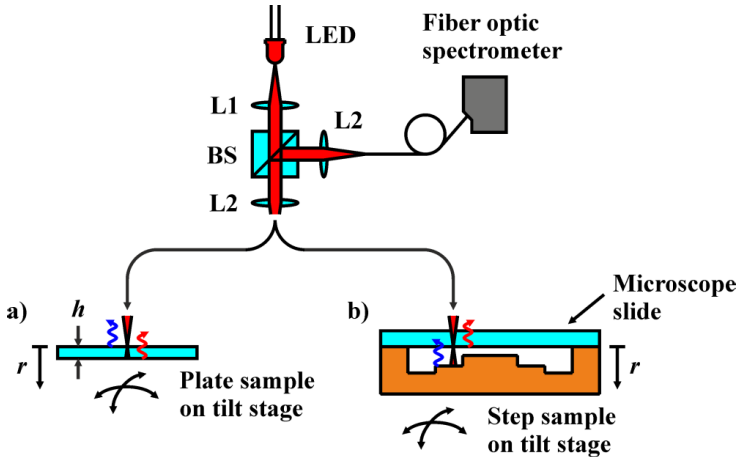


Figure 5 Schematic of the spectrometer FDSCI setup for thickness measurement of the plate sample (a) and for step profile measurement (b). Blue (external reflection) and red (internal reflection) wave arrows indicate the interfering reflections. Abbreviations: LED, light emitting diode; L, lens; BS, beam splitter; r , optical length; h , optical thickness.

Time domain interferometry differs from its Fourier domain counterpart by the fact that the detector measures the spectrally unresolved intensity of the interfering reflections; that is, $I(k)$ integrated over k . To reveal a time domain interferogram, either the reference mirror is scanned across the sample mirror, or the sample mirror is scanned across the reference mirror, as is typical in scanning white light interferometry. For parallel light, the coherence function that describes the detected intensity as a function of the scan, r , is [6]

$$I(r) = \int_0^\infty \left[\frac{1}{4} S(k) [P_R(k) + P_S(k)] + \frac{1}{2} S(k) \sqrt{P_R(k) P_S(k)} \cos[2k(r - n_p(k) D_s)] \right] dk. \quad (3)$$

The time domain A-scan is an interference burst riding on a DC component. The maximum of the envelope of the interference burst is at $r = n_g(\lambda_0) D_s$. In time domain interferometry, this scan position measures length.

Resolution, i.e., the smallest distance between two separable interference signals, is limited by the coherence length. The coherence length is a property of the light source, which is calculated by assuming a Gaussian spectral distribution,

$$l_c = \frac{2 \ln 2}{\pi} \frac{\lambda_0^2}{\Delta \lambda}, \quad (4)$$

where $\Delta \lambda$ is the -3 dB bandwidth of the light source [6]. For broadband light sources, like those used in this thesis, the coherence length is short, and therefore the term “short coherence interferometry” is used.

The visibility of the interference signal is limited by the light intensity reflected from the reference and from the sample mirrors, I_R and I_S . The maximum interference visibility, ν , relative to the DC component is

$$\nu = \frac{2S\sqrt{P_R P_S}}{S[P_R + P_S]} = \frac{2\sqrt{I_R I_S}}{I_R + I_S}. \quad (5)$$

Equation (5) indicates that the maximum visibility of 1 is achieved when the reflected intensities are equal. In the literature the term “low coherence interferometry” is frequently used; however, this term is somewhat misleading since “low” refers to poor visibility of the interference fringes. The same maximum interference visibility is found at equal reference and sample optical path length, regardless of the coherence length.

Paper IV accounted for nonidealities arising from the objective’s numerical aperture, NA, (converging light beam) [12, 13], and from light scattering from random rough surfaces in the system [14-19]. These effects modify the coherence function and need to be considered when measuring samples with complex structures like steps, layers, gratings, and vibrating surfaces (could be treated as a distributed surface height over time).

4 FDSCI SETUP TO CHARACTERIZE CLIC-AS INTERNAL ALIGNMENT

Fourier domain interferometry was chosen rather than time domain interferometry because it requires no moving parts and no accurately position encoded reference mirror. Requiring no moving reference mirror, a Fourier domain short coherence interferometer (FDSCI) can rapidly do absolute length characterization point-by-point across a measurement range exceeding 10 mm [20].

Fourier domain interferometry is a standard technology in optical coherence tomography, used in applications such as biomedical imaging of the eye [21, 22] and endoscopy [23, 24]. Metrological FDSCI instruments [20, 25] have been used to characterize the surface metrology of hard-to-reach solid objects. Scanning white light interferometry (SWLI) that applies the time domain principle is employed in bioimaging [26] and in surface metrology, where it provides submicron accuracy [27]. Coherent light instruments, such as two-wavelength heterodyne interferometers [28], provide nanometer accurate displacement data. However, when quantifying a discontinued surface profile in the millimeter range, the phase ambiguity corrupts the length measurement.

Our solution to quantify the internal alignment of an accelerating structure (AS) of the Compact Linear Collider (CLIC) is an FDSCI setup calibrated to submicron accuracy with methods familiar from SWLI [27, 29]. We developed the setup in steps. First, a proof of concept and the required length calibration aspects were worked out using a spectrometer FDSCI setup that employed free-space optical components and featured a short measurement range. In the second development phase, a fiber-optic FDSCI setup based on a tunable fiber Fabry-Perot spectral filter was built. During the second phase we extended the measurement range beyond the AS-cavity radius and integrated a fiber-optic probe to access the hard-to-reach AS-cavity.

4.1 SPECTROMETER FDSCI

Figure 5 shows the spectrometer FDSCI setup. Light from a light emitting diode (LED: Kingbright, L-793SRC-E, $\lambda_0 = 655$ nm and $\Delta\lambda = 22$ nm at 20 mA forward current) was collimated by lens 1 and focused onto a sample by lens 2 (L1 and L2: Thorlabs, ACL2520-B, diam. = 25.0 mm, $f = 20$ mm). Glass coverslip and plastic shim samples for calibration purposes are described in detail in paper I, and a copper step sample to show proof of concept for AS alignment is described in paper III. The light reflected back was coupled using a cube beam splitter (BS: Optosigma, 039-0265) and

lens 3 (L3: Thorlabs, LA1805-B, diam. = 25.4 mm, $f = 29.9$ mm) into a visible range fiber-optic spectrometer (Ocean Optics, HR2000+, spectral resolution $\delta\lambda = 0.44$ nm). Although it sounds confusing, the notation, “capital delta lambda, $\Delta\lambda$ ” for the -3 dB bandwidth and “lower case delta lambda, $\delta\lambda$ ” for the spectral resolution, is common in the optical coherence tomography literature and is used in this thesis too. The spectrometer captured the spectral interference data. In calibration plate samples, the interference was constructed from the front and rear surface reflections of the sample, Fig. 5(a). A 1 mm thick microscope slide was placed on top of a copper step sample, Fig. 5(b), to provide a reference reflection that interfered with the sample reflection. Both measurements employed the common-path technique. In Fig. 5(a, b) the interfering reflections are indicated by blue (external reflection) and red (internal reflection) wave arrows. Perpendicular alignment of the sample against the optical axis was ensured to better than 7.0 mrad by maximizing the recorded intensity.

A-scans were extracted from the spectral interferograms, Fig. 6, using an inverse fast Fourier transform (IFFT). As the spectrometer acquires data in wavelength space, λ , the data was first transformed into k -space. Since the wavenumber is nonlinearly proportional to the wavelength, $k = 2\pi/\lambda$, the IFFT cannot be done directly without distorting the shape of the A-scan (nonlinear k -space sampling causes apparent system dispersion that alters the shape of the interference signal). A way to resample the data into equispaced k is to convolve the acquired data with a Gaussian interpolation kernel [30]. A-scans can then be calculated using IFFT on the resampled data and by deconvolving the A-scans with the IFFT of the interpolation kernel. This method to linearize the wavenumber domain interferograms is software-based, and therefore, requires no complex prism [31] to compensate for the uneven dispersion at the detector array of the spectrometer.

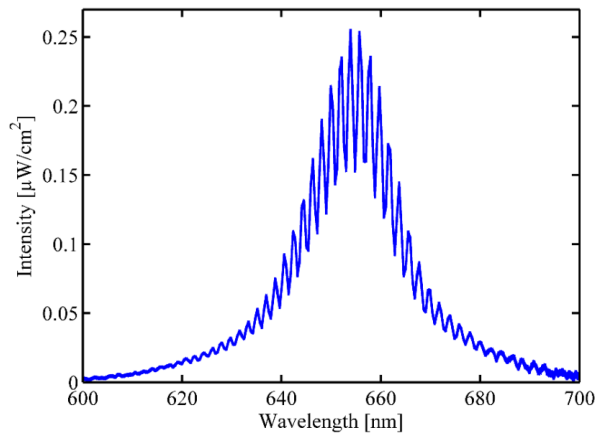


Figure 6 Spectral interferogram of a glass coverslip sample measured using the spectrometer FDSCI setup. 100 spectral interferograms on top of each other are shown.

A-scans of three glass coverslips and one plastic shim sample are shown in Fig. 7. The amplitude of the coherence function was normalized to the DC peak at zero optical length for each sample. Based on the Nyquist sampling criterion [6], the finite spectral resolution, $\delta\lambda$, of the spectrometer limits the maximum optical measurement range to

$$r_{\max} = \frac{\lambda_0^2}{4\delta\lambda}. \quad (6)$$

In our spectrometer FDSCI setup, $r_{\max} = 240 \mu\text{m}$. The axial pixel size, i.e., the bin width of the r -axis, was adjusted to 2 nm by zero padding the resampled spectral interferogram [32]. The axial resolution, quantified as the half width of the A-scan interference peak, equals $7.4 \mu\text{m}$ and is close to the coherence length, Eq. (4), of a Gaussian light source, $8.6 \mu\text{m}$. The measured optical thickness, h_M , of the plate samples or the measured optical length, r_M , between the copper sample surface and the reference surface were determined as the location of the energy centroid (interference peak's maximum position). In 100 A-scans the repeatability ranged from 4.6 to 200 nm at 95% confidence level. The reduced repeatability is caused by the limited amplitude of the interference signal. In Fourier domain interferometers, the amplitude of the interference signal exhibits length dependent falloff because of: 1) the finite spectral resolution, 2) interpixel crosstalk in the detector array of the spectrometer, and 3) nonlinear k -space sampling [33]. The spatial coherence of the reflected light reduces the interference amplitude as well [34]. In addition, the signal-to-noise ratio (SNR) of the spectrometer (at full exposed signal) limits the noise floor in A-scans to -23 dB . The noise floor increases for long measurement ranges, due to A-scan deconvolution associated with k -space resampling [30].

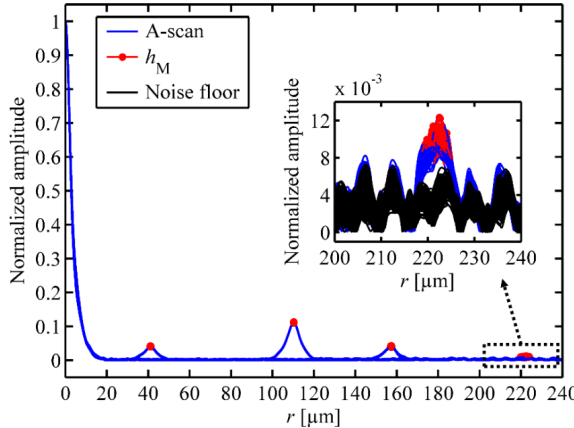


Figure 7 Spectrometer FDSCI A-scans of three glass coverslips ($h_M = 110 \mu\text{m}$, $157 \mu\text{m}$, and $222 \mu\text{m}$) and one plastic shim sample ($h_M = 41 \mu\text{m}$). A-scan amplitude normalized to the DC peak at zero optical length. A-scans repeated 100 times for each sample. Inset: Close-up view into the weakest perceived interference peak. Abbreviations: r , optical length; h_M , measured optical thickness.

4.2 FIBER-OPTIC FDSCI

Figure 8 shows the fiber-optic FDSCI setup. Light from a pulsed near infrared LED (Qphotonics, QFLED-1550-20, nominal $\lambda_0 = 1550$ nm, nominal $\Delta\lambda = 60$ nm, 80 mA forward current, 12 kHz pulsing frequency, 50% duty cycle) was directed through an optical circulator (C: Thorlabs, 6015-3-FC) into a fiber-optic probe that was inserted into the AS-cavity. The fiber-optic probe comprises a single mode fiber (SMF: Thorlabs, SMPFo215-FC, NA = 0.14, antireflection coating removed), a gradient index lens (GRIN: Edmund Optics, #64531, 0.25 pitch, $f = 1.73$ mm), a right angle prism (RAP: Edmund Optics, 32525, side length = 2 mm), and a carbon fiber housing (Excel, diam. = 3.85 mm, length = 300 mm). To collimate light, SMF and GRIN were glued together using an optical adhesive (Norland Products Inc., NOA61). The right angle prism was glued to the GRIN to achieve a 90° side view. A 500 μm spot diameter and 3.0 mrad acceptance angle at a $1/e^2$ level of maximum intensity are predicted by ray tracing simulations. The fiber-optic probe operates in common-path configuration: The end surface of the right angle prism provides the reference reflection for interferometry. In Fig. 8 the interfering reflections are indicated by blue and red wave arrows.

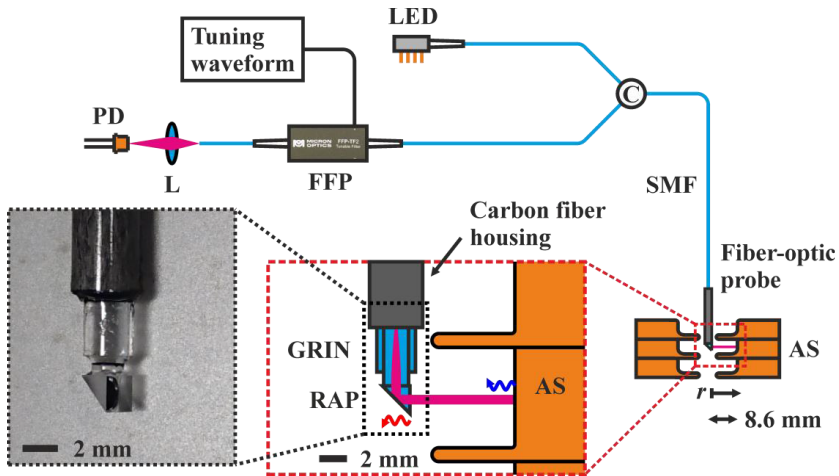


Figure 8 Schematic of the fiber-optic FDSCI setup for AS internal alignment measurement. Right inset: Close-up view of the fiber-optic probe and AS internal measurement. The end surface of the right angle prism provides a reference reflection, red wave arrow, for interferometry. Sample reflection indicated by blue wave arrow. Left inset: Photograph of the fiber-optic probe. Abbreviations: LED, light emitting diode; C, optical circulator; SMF, single mode fiber; GRIN, gradient index lens; RAP, right angle prism; AS, accelerating structure; FFP, fiber Fabry-Perot spectral filter; L, lens; PD, photodetector; r , optical length.

Sample and reference reflections were directed into a tunable fiber Fabry-Perot spectral filter (FFP: Micron Optics, FFP-TF2, 234.6 nm free spectral range and $\delta\lambda = 0.023$ nm pass band linewidth at 1550 nm wavelength). The pass band filtered light was focused by a lens (L: Thorlabs, C230TMD-C, $f = 4.51$ mm) into a photodetector (PD: Roithner LaserTechnik, PT511-2 + transimpedance amplifier, 47 kHz bandwidth) that captured the spectral interferogram. Because of the narrow bandwidth of the photodetector, the FFP was driven with reduced performance [20]: A triangular tuning waveform, with 0.7 Hz frequency and 210 mV_{pp} amplitude, was used. As a result, the pass band was swept across a reduced spectral range of 28 nm with reduced effective spectral resolution (pass band linewidth affected by the PD bandwidth) limiting the measurement range. The DC level of the tuning waveform was adjusted for maximum pass band intensity. An interferogram from a silver mirror as a function of the tuning waveform index is shown in Fig. 9.

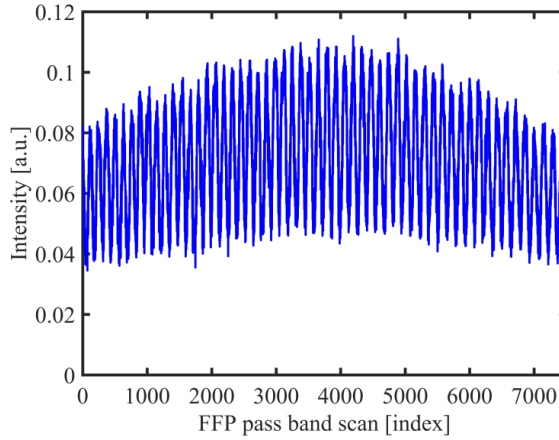


Figure 9 Spectral interferogram of the fiber-optic FDSCI setup shown as a function of the fiber Fabry-Perot spectral filter (FFP) tuning waveform index.

The pass band sweep of the piezo actuated FFP is nonlinear in k . To resample the acquired spectral interferograms into equispaced k , a structure linear in wavenumber is needed [35]. Interference in a nondispersive medium, i.e., $n_p(k) = \text{constant}$, is one such structure. Air can be considered nearly nondispersive, since the refractive index of air changes less than 10^{-7} across the bandwidth of the light source. This causes negligible phase nonlinearity. First, an inverse fast Fourier transform and boxcar filter are performed on the k nonlinear interferograms to remove A-scan peaks other than the interference peak in the air medium [21]. The remaining data is then fast Fourier transformed back to the k nonlinear space to analyze the phase nonlinearity. A third order polynomial is fitted to the unwrapped phase to determine linear k indexing for the acquired spectral interferograms [36].

The k linear interferograms are obtained by resampling the acquired spectral interferograms to the linear k indexing. A-scans are finally extracted from the resampled spectral interferograms by IFFT. The horizontal axis of the A-scans represents the optical length. Before calibration, it is shown as an index without length unit.

A-scans of a silver mirror, placed at a 1.3 – 9.3 mm probe-to-mirror distance with 1 mm increments, are shown in Fig. 10. The linear k -space resampling was done with the same resampling parameters used with the 1.3 mm data point. The amplitude of the coherence function was normalized to the DC peak at zero optical length for each A-scan. The measured optical lengths were determined as the location of the energy centroid of the A-scans. The measurement range exceeded the 8.6 mm range required for the AS-cavity measurement. However, the low bandwidth of the photodetector limited the maximum measurement range of the setup to below the maximum range achievable by the FFP, 25.3 mm estimated by Eq. (6). As well, the axial resolution was 50 μm , whereas the coherence length, Eq. (4), of the light source was 20 μm . Further, the low optical power of the LED (20 μW at 67 mA continuous forward current) limited the SNR to 25 dB. Other sources which affect the interference amplitude are those described for the spectrometer FDSCI setup. The measurement range and the axial resolution could be maximized to 25.3 mm and 20 μm , respectively, by increasing the optical power of the light source. With higher optical power, lower gain in the photodetector is required, and therefore a photodetector with wider bandwidth could be used. With this, the pass band sweep could be extended across the light source spectrum with an effective spectral resolution equal to the pass band linewidth of the FFP.

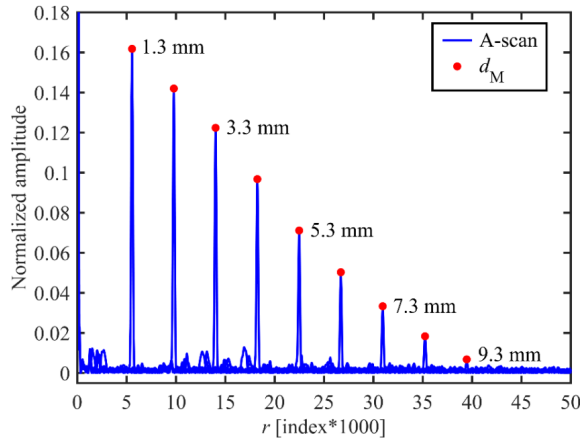


Figure 10 Fiber-optic FDSCI A-scans of a silver mirror at 1.3 – 9.3 mm probe-to-mirror distance. Prior to length calibration, the horizontal axis of A-scans is shown as an index without length unit. A-scan amplitude normalized to the DC peak at zero optical length. Abbreviations: r , optical length; d_M , measured optical distance.

Unstable operation of the FFP and vibration of the fiber-optic probe raises instability in the fiber-optic FDSCI setup. To test the length stability of the fiber-optic FDSCI setup during prolonged measurements, the distance to a stable glass plate (3.2 mm thick) placed ca. 2 mm from the probe end in air was monitored for one hour. Each spectral interferogram was resampled to linear k -space with individual resampling parameters, i.e., coefficients of the polynomial fit [21]. The stability test was repeated three times by restarting the setup and readjusting the DC level of the FFP tuning waveform. Figure 11(a) shows the measured probe-to-glass plate optical distance, d_M , averaged over a 27 sec sliding window. A 45 min stabilization time caused by creep of the DC level of the FFP tuning waveform was found. Once stabilized, d_M varies by 30 indices, corresponding to 7 μm , caused by pass band sweep instability [37] and phase jumps in the unwrapped phase data. Further, d_M always stabilizes to a different level after restarting the setup. In the third restart repeat, d_M and the optical thickness of the glass plate, h_M , were quantified simultaneously. Figure 11(b) shows h_M and d_M , with a significant correlation between them, $r_{\text{corr}}(h_M, d_M) = 0.998$. This suggests pre-calibrating A-scans to a stable optical length to reduce the FFP induced instability. Figure 11(c) shows d_M pre-calibrated to the physical optical thickness of the glass plate with a nominal group refractive index of 1.5, $h_M = 3.2 \text{ mm} \cdot 1.5 = 4.8 \text{ mm}$. Using 100 A-scan sliding window, the repeatability, affected by the vibration of the fiber-optic probe, was better than 0.2 μm at a 95% confidence level. No length drift was observed after 10 minutes from the restart.

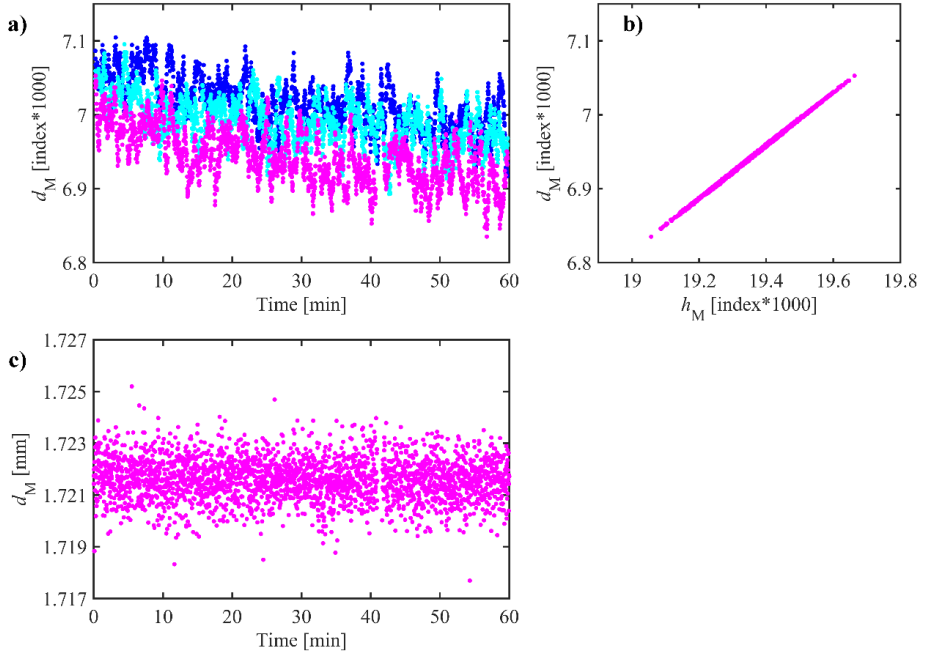


Figure 11 Stability test of the fiber-optic FDSCI setup. (a) Measured and 27 sec sliding window averaged optical distance, d_M , of a stable 3.2 mm thick glass plate placed ca. 2 mm from the probe end, monitored for 1 hour. The stability test was repeated three times by restarting the setup: ●, repeat 1; ●, repeat 2; ●, repeat 3. (b) Simultaneous quantification of d_M and optical thickness of the glass plate, h_M , in the third restart repeat. Prior to length calibration, the optical lengths measured are shown as an index without length unit. (c) d_M pre-calibrated to the physical optical thickness of the glass plate with a nominal group refractive index of 1.5, $h_M = 3.2 \text{ mm} \cdot 1.5 = 4.8 \text{ mm}$.

5 LENGTH CALIBRATION

In general, calibration [38] derives a measurement result from an indication (uncalibrated measure). First the calibration establishes a relation between the quantity values of measurement standards and their corresponding indications with measurement uncertainties [38] that characterize the dispersion of values attributed to the measurand. This relation is the calibration function. In good practice, this relation is quantified by measuring at least five measurement standards. The quantity values of the measurement standards and their corresponding indications are compared to determine the measurement bias. Then a calibration function of justified functional form is fitted in least squares manner to the measurement bias data to obtain the calibration constant(s) of the calibration function with uncertainties. In the second step this calibration function is used to remove the measurement bias from an indication, i.e., to derive a measurement result from an indication.

In this thesis, the length calibration is conducted by comparing the measured optical thickness of a plate standard to the certified geometric thickness translated by the group refractive index of the plate standard. Sources of uncertainty include the plate standard, measurement repeatability, sample orientation, thermal expansion, and group refractive index of air.

5.1 LENGTH TRANSFER STANDARD

A length transfer standard is a secondary standard that has been compared to the national length standard, a realization of the definition of the meter. The calibration chain may contain several transfer standards. A length transfer standard has a documented geometric length and a documented unbroken chain of calibrations, each contributing to the measurement uncertainty (traceability) [38].

In scanning white light interferometry (SWLI) the length calibration is typically conducted by measuring a step standard [27, 29]. Length calibration of a point-by-point detection Fourier domain interference profilometer by a step standard requires lateral translation to obtain a step profile. Unfortunately, such translation induces extra uncertainty sources that inflate the final measurement uncertainty. Length calibration through transparent transfer standards, e.g. glass plates, overcomes this issue, as an absolute optical length measure is quantified without any translational scanning device. Therefore, we consider transparent standards more feasible for FDSCI length calibration than step standards.

In paper I, two plastic shim thickness standards (Check Line, CPS-100, SCU-100-0041; #11441, $(11 \pm 1) \mu\text{m}$; and #11442, $(23 \pm 1) \mu\text{m}$) and three standard thickness coverslips (Schott, D 263® M; #00; #0; and #1) were used as length transfer standards to calibrate the Fourier domain short coherence interferometer (FDSCI) setup. Coverslips were chosen, since they are stable (temperature coefficient of the refractive index $\sim 10^{-6}/\text{K}$, linear coefficient of thermal expansion $\alpha = 7.2 \cdot 10^{-6}/\text{K}$) and flat, which makes them ideal as transfer standards. The calibrated geometric thickness, H_c , of the coverslips was quantified using a Hitachi S4800 scanning electron microscope (SEM) that was calibrated at $400\times$ magnification by a cross-ruled calibration specimen (SIRA SEM S170, 19.7 lines/mm, 1% accuracy, Fig. 12 inset) at 10 kV, 10 μA , and 23.4 mm working distance. The H_c was quantified from cross-sectional SEM images, Fig. 12, by fitting a normal to the lower and upper edge of the coverslip and by counting pixels from edge to edge along the normals. Perpendicular alignment between the coverslip and SEM image plane was ensured to better than 1.7 mrad by adjusting the tilt of the sample holder inside the SEM chamber.

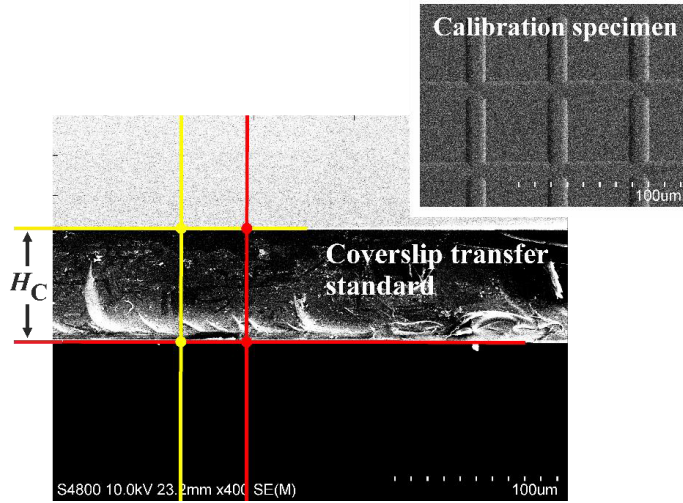


Figure 12 Scanning electron microscope image of cross-section of #00 coverslip transfer standard. H_c , calibrated geometric thickness. Inset: Cross-ruled calibration specimen, 19.7 lines/mm, 1% accuracy, SIRA SEM S170.

For the length calibration of the fiber-optic FDSCI we propose 0.1 – 10 mm thick fused silica plate transfer standards (temperature coefficient of the refractive index $\sim 10^{-5}/\text{K}$, linear coefficient of thermal expansion $\alpha = 0.55 \cdot 10^{-6}/\text{K}$). The thickness of gauge blocks is typically calibrated against a helium-neon laser interferometer [39, 40]. Alternatively, at CERN Metrology, the H_c could be quantified using a calibrated coordinate

measuring machine (CMM) [4]. Thickness accuracy on the order of $0.1 \mu\text{m}$ is expected.

Another option to calibrate a Fourier domain interferometer is to use at least two separate spectral line features, e.g., laser emissions, fiber Bragg gratings, or atomic spectroscopy emission lines, with known wavelengths [41]. In the length calibration hierarchy, stabilized laser sources, called line standards, are above the step and plate standards, and therefore they would provide the most accurate length calibration. However, for practical use, the step and plate standards are most convenient because of their ease of use, dimensional stability, and low cost.

5.2 REFRACTIVE INDEX

The absolute (not relative to air) group refractive index, n_g , of the plate transfer standard needs to be known to convert the documented geometric thickness into optical thickness. Several methods to measure the refractive index of solids exist. Refractometers, based on measuring the critical angle or the angle of refraction, are limited by sample size and shape, and they require a predefined scale in order to read the index value [42, 43]. Polarimetric [44] and surface plasmon resonance [45] methods are sensitive, but employ cumbersome models to extract the dielectric function of the sample. Interference microscope methods can quantify the group refractive index [27, 46, 47]. However, their accuracy relies on calibrated interference and confocal scanners and on the objectives' working numerical aperture (NA). In contrast, a Fourier domain Mach-Zehnder interferometer measures the group refractive index without moving parts [48]. To have accurate results, the two light beams of the Mach-Zehnder interferometer need to be balanced, i.e., the optical path lengths of the interfering light beams are set equal, which is difficult because the two light beams share no optical components.

The phase refractive index, n_p , of a medium is defined as the ratio between the phase velocity of light in vacuum and in the medium, which is a dimensionless quantity. The quantities n_g and n_p are related to each other through the expression

$$n_g = n_p - \lambda \frac{dn_p}{d\lambda}, \quad (7)$$

where λ is the wavelength of light in a vacuum. This expression neglects higher order dispersion when attributed to finite bandwidth light. The group velocity dispersion depends on the light source bandwidth and on the sample thickness [5]. Therefore, for the proposed $0.1 - 10 \text{ mm}$ thick fused silica plate transfer standards, no valid group refractive index can be deduced from the phase index data. A direct measurement of n_g is required.

In paper II we demonstrated n_g quantification for transparent samples using a Sagnac type FDSCI. Two standard thickness coverslips, #00 and #0,

were used as samples. Figure 13 depicts the setup. Shortly, light from a light emitting diode (LED) was coupled into a multimode fiber, then collimated, and stopped to ca. 1 mm beam diameter. This collimated input light beam was directed into a Sagnac type interferometer, Fig. 13 (dashed box), constructed from a beam splitter and two silver mirrors. In this configuration the input light was split into clockwise and counterclockwise light beams which were steered back into the beam splitter by two mirrors. The recombined Sagnac output beam was fed into the fiber-optic spectrometer, which recorded the spectral interference data. The two light beams in the Sagnac interferometer were balanced to zero optical path length difference with the help of interference: Close to complete beam recombination, interference modulation was achieved, and the zero difference was found by adjusting the mirrors to maximize the recorded intensity. The two beams were balanced in a displaced configuration. This is beneficial, because if the sample partly cuts both beams, the measurement result is biased in a way that depends on the beam footprints and on the beam orientations. We avoided this bias by placing the sample so that it cut only one of the beams.

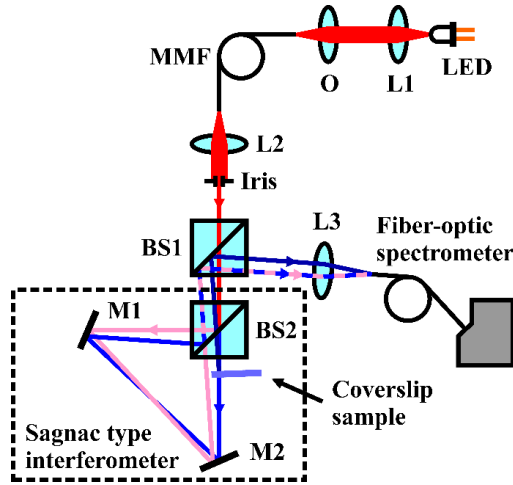


Figure 13 Sagnac type FDSCI setup to determine the group refractive index. The dashed box highlights the Sagnac type interferometer configuration. LED, light emitting diode; L, lens; O, objective; MMF, multimode fiber; BS, beam splitter; M, mirror; —, input light beam; —, clockwise light beam; —, counterclockwise light beam; —, Sagnac output light beam; —, sample reflections.

The coverslip samples were placed into the clockwise beam path in a slightly slanted orientation, $< 2^\circ$, (0.2° acceptance angle) to capture sample reflections with the same fiber-optic spectrometer. The coverslip modifies the clockwise beam path and generates two distinctive interference peaks, Fig. 14. Peak h , Fig. 14 (right inset), measures, under a small angle approximation, the optical thickness, h , of the sample. Peak s accounts for

the optical path length difference between the modified beam path and the unmodified counterclockwise beam path. Because the measured lengths are half of the corresponding optical path lengths, the added optical path length equals the measured s multiplied by 2. This difference describes the added optical path length in the modified beam path, where the path through the sample of geometric thickness, H , and group refractive index $n_{g, \text{sample}}$ replaces a corresponding path in air. Under the small angle approximation we get

$$2s \approx n_{g, \text{sample}} H - n_{g, \text{air}} H = h - n_{g, \text{air}} H. \quad (8)$$

From Eq. (8) the geometric thickness of the sample is

$$H \approx \frac{h - 2s}{n_{g, \text{air}}}. \quad (9)$$

The group refractive index of the sample is calculated as a ratio between the optical and geometric thickness of the sample

$$n_{g, \text{sample}} = \frac{h}{H} \approx \frac{h}{h - 2s} n_{g, \text{air}}. \quad (10)$$

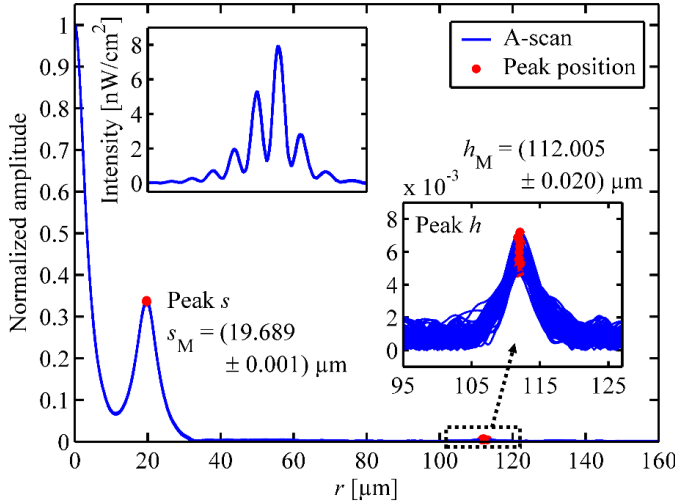


Figure 14 Sagnac type FDSCI A-scan reveals the optical thickness of the #00 coverslip sample, peak h , and the Sagnac beam path difference, peak s . h_M and s_M represent the measured lengths. A-scan amplitude normalized to the DC peak at zero optical length, r . Insets: Peak h close-up view (right inset); spectral interferogram, indexed wavenumber data, 100 repeats (left inset).

The linear k -space resampling was done on an interference signal from a $50 \mu\text{m}$ thick air gap, according to the procedure introduced for the fiber-optic FDSCI setup. The nominal $50 \mu\text{m}$ air gap thickness was used to scale the horizontal axis of the A-scans. In the Sagnac interferometer, Fig. 13 (dashed box), the dispersion of the optical components was effectively matched

because the two counter propagating light beams were balanced and they shared the same optical components. The measured lengths, h_M and s_M , were extracted from repeated A-scans ($N = 100$), Fig. 14, the left inset showing the recorded spectral interferograms. The group refractive index of the sample was then quantified from these two length measures using Eq. (10). The results are shown in section 6.1.

The group refractive index of air was evaluated using the Edlén equation [49] and the expression for the group refractive index, Eq. (7),

$$n_{p, \text{air}}(\lambda_0) = 1 + \frac{p}{96095.43} \left[\left(8342.54 + \frac{2406147}{130 - \lambda_0^{-2}} + \frac{15998}{38.9 - \lambda_0^{-2}} \right) \cdot 10^{-8} \right] \cdot \left[\frac{1 + (0.601 - 0.00972T)p \cdot 10^{-8}}{1 + 0.0036610T} \right] - f_{pp} (3.7345 - 0.0401\lambda_0^{-2}) \cdot 10^{-10}, \quad (11)$$

where p is the atmospheric pressure in Pa, T is the ambient temperature in °C, λ_0 is the central wavelength of the light source in μm , and f_{pp} is the water vapor partial pressure in Pa. Moreover, f_{pp} is related to the relative humidity, H_R , by $f_{pp} = H_R f_{\text{sat}}$, where f_{sat} is the water vapor partial pressure of saturated moist air. f_{sat} was calculated using the Buck equation [50]

$$f_{\text{sat}} = (1.0007 + 3.46p \cdot 10^{-8}) \cdot 6.1121 \exp\left(\frac{17.502T}{240.97 + T}\right), \quad (12)$$

where p and f_{sat} are in Pa, and T in °C. In our measurements T and H_R were recorded using a data logger (Clas Ohlson, 36-4208-1/ST-171), whereas p was recorded using a pressure sensor (Vaisala, PTB100A). The uncertainty associated with Eq. (11) that describes the phase refractive index of air is on the order of 10^{-8} and it is valid in standard laboratory atmospheric conditions across the 350 nm to 650 nm range of wavelengths [49]. A broader range of validity is given by Ciddor [51]. Despite the high accuracy of Eq. (11), the uncertainty of $n_{g, \text{air}}$ is dominated by the typical accuracy of atmospheric sensors and atmospheric fluctuations: temperature $\pm 1^\circ\text{C}$, relative humidity $\pm 3\%$, and atmospheric pressure ± 15 Pa. $n_{g, \text{air}}$ is most sensitive to temperature uncertainty; therefore, an uncertainty in the refractive index of air of 10^{-6} is expected.

5.3 COSINE ERROR

Interferometric devices measure length along the direction of light propagation, i.e., along the optical axis. If this axis is slanted with respect to the normal of the sample surface, a cosine error [52] is generated. For parallel light, any misalignment between the optical axis and the sample normal causes the measured optical thickness to exceed the actual optical thickness along the normal. The cosine error corrected length, L , for a tilted sample, Fig. 15 (left), marked by a prime, is

$$L'_M = L_M \cos \theta = L_M \left(1 - \frac{\theta^2}{2} \right), \quad (13)$$

where θ is the angular error between the measurement axis and the sample normal. The right side of the equation presents the first two terms in a Taylor series.

Another type of cosine error arises when light is focused onto a sample. In this case, no single angle represents the optical axis, and the analysis needs to take into account the entire angular aperture range appropriately weighted by the corresponding light intensities [12]. An aperture function, f_{NA} , that corrects the quantified optical measure for the convergence of the light beam under the small angle approximation is [12]

$$f_{NA} = \frac{1 + \cos \theta_{\max}}{2}, \quad (14)$$

where the cone angle of the light beam, θ_{\max} , is related to the objective's NA by $\theta_{\max} = \sin^{-1}(NA)$, and uniform illumination on the back aperture of the objective lens is assumed. Other aperture functions have been discussed, e.g., Creath [13].

In practice, optical systems are further affected by wavefront errors caused by sample flatness and imaging aberrations. Thus, in real optical systems, analysis of the cosine errors discussed above is complex. One way to overcome this issue is to measure the optical thickness at several sample tilt angles across the acceptance angle of the system. The uncertainty associated with sample orientation is then evaluated as the maximum change in the measured optical thickness. This maximum uncertainty includes the optical lengths of all sample orientation scenarios within the acceptance angle of the system. This approach benefits from the fact that the complex mechanism of propagation of uncertainty caused by the cosine and wavefront errors does not need to be explicitly known. The associated uncertainty increases with increasing acceptance angle. Thus, to reduce this uncertainty, the acceptance angle needs to be reduced, which, in practice, has a lower limit defined by the size of the light source [53]. In fiber optics, the acceptance angle is limited by the mode field diameter.

In scanning electron microscope (SEM) measurements, the measured geometric thickness of the sample is a projection of the actual geometric thickness onto the image plane of the SEM. This causes the measured thickness to appear shorter than the actual thickness. For projection, Fig. 15 (right), the length, L , corrected for the cosine error is

$$L'_M = \frac{L_M}{\cos \theta} = L_M \left(1 + \frac{\theta^2}{2} \right). \quad (15)$$

Again, the first two Taylor series terms are given.

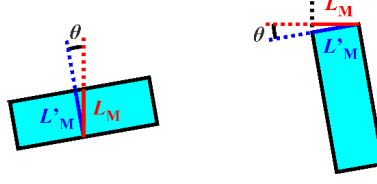


Figure 15 Principle of cosine error due to sample tilt (left) and projection (right). Abbreviations: θ , angular error; L_M , measured length; L'_M , cosine error corrected length.

5.4 THERMAL EXPANSION

Thermal expansion describes how much the length dimensions of a solid object change with temperature. Thus, when comparing the length of an object measured at different temperatures, the thermal expansion needs to be taken into account. The length of the object at a certain temperature different from the reference temperature is [54]

$$L_{\Delta T} = L(1 + \alpha \Delta T), \quad (16)$$

where ΔT is the temperature difference, L is the initial length of the object, and α is the linear coefficient of thermal expansion.

5.5 LENGTH CALIBRATION FUNCTION OF FDSCI

A linear length calibration function is justified for the FDSCI. The dilation property of the Fourier transform [55] ensures that any error in bin width in the equispaced k -space dilates the length space linearly. Thus, the calibration function, C , of any Fourier domain interferometer is linear with respect to the optical length, r , that is

$$C = ar, \quad (17)$$

where a is the calibration constant. This requires that the recorded spectral interferograms are appropriately resampled into linear k -space. We would also need to compensate for the dispersion of the optical components of the system (except for the sample medium itself). We do this by employing the common-path technique and a balanced Sagnac interferometer configuration (for n_g quantification). The calibrated optical length, r_c , is calculated as

$$r_c = r - C. \quad (18)$$

6 RESULTS

6.1 GROUP REFRACTIVE INDEX QUANTIFICATION

The group refractive index, n_g , quantification of transparent samples, using the Sagnac type FDSCI, is the main result of paper II. In this method (section 5.2) the group refractive index of transparent samples was quantified from two length measures, 1) the optical thickness of the sample, h_M , and 2) the Sagnac beam path difference, s_M , using Eq. (10). Taking the length calibration, Eq. (17, 18), into account, the calibrated measures, h_{CM} and s_{CM} , become $h_M(1 - a)$ and $s_M(1 - a)$. Evaluating $n_{g, \text{sample}}$ by using the calibrated measures, h_{CM} and s_{CM} , the calibration constant, a , cancels out and an accurate $n_{g, \text{sample}}$ result is evaluated directly from the uncalibrated measures, h_M and s_M . This allows us to quantify n_g of the plate transfer standards prior to the length calibration.

The measurement gave $n_{g, \text{sample}} = 1.5426 \pm 0.0042$ for the #00 coverslip sample and 1.5434 ± 0.0046 for the #0 coverslip sample at $\lambda_o = 658$ nm. The uncertainties are quoted at 95% confidence level and combine contributions from random uncertainties in sample orientation, h_M , and s_M , and from systematic uncertainties arising from $n_{g, \text{air}}$ and balancing that were common for the two samples. The uncertainties were evaluated using the Guide to the expression of uncertainty in measurement [56]. Table 1 summarizes the uncertainty budget for the #00 coverslip sample. Standard uncertainties for h_M and s_M , and the correlation between them, $r_{\text{corr}}(h_M, s_M)$, were obtained from repeated A-scans, $N = 100$. The uncertainty contribution associated with sample orientation was estimated as the maximum change in $n_{g, \text{sample}}$ as the sample was tilted across the 0.2° acceptance angle of the system. In addition, the slanted sample orientation causes a biasing cosine error. However, for a 2° slanted sample, this bias is on the order of 10^{-4} , which can be neglected in the analysis. The thermal instability of measurements was within 1°C , and this affects the refractive index of borosilicate glasses like Schott D 263® M on the order of 10^{-6} . Thus, the thermal instability was also neglected. Finally, since variation in the Sagnac interferometer balancing causes zero centered variation in the balanced optical path length difference, the systematic balancing uncertainty was estimated by measuring the variation in s when the balancing was repeated 10 times.

As expected, the group refractive index measurement of #00 and #0 coverslip samples shows overlapping results, since both samples were produced from the same glass material. In addition, using Eq. (7), the phase refractive index data of the glass material gives $n_g = 1.5445$ at $\lambda_o = 658$ nm. Because of the narrow band light emitting diode (-3 dB bandwidth 21 nm) and small sample thickness (70 μm and 100 μm), the group velocity dispersion has only a minor effect on the quantified n_g . For these samples,

the quantified n_g could thus be considered consistent with Eq. (7). The result derived from the phase index data is within the measurement uncertainty of n_g and verifies the validity of the presented method.

Table 1. *Group refractive index uncertainty budget for the #00 coverslip sample. The total uncertainty was obtained as the root sum of squares from the random and systematic uncertainty components. The most important value is bolded.*

Uncertainty component	Unit	Value	Standard uncertainty		Sensitivity coefficient	Contribution	
			$u(x_i)$		$c_i = \frac{\partial f}{\partial x_i}$	$u_i(y) = c_i u(x_i)$	
			Rand.	Sys.		Rand.	Sys.
Measured optical thickness	h_M	μm	112.005	0.020	$-\frac{2s_M}{(h_M - 2s_M)^2}n_{\text{g, air}}$	$1.5 \cdot 10^{-4}$	
Sagnac beam path difference	s_M	μm	19.689	0.001	$\frac{2h_M}{(h_M - 2s_M)^2}n_{\text{g, air}}$	$3.9 \cdot 10^{-5}$	
Sample orientation						$2.1 \cdot 10^{-3}$	
Group refractive index of air	$n_{\text{g, air}}$	-	1.00027427	$5.2 \cdot 10^{-7}$	$\frac{h_M}{h_M - 2s_M}$		$8.1 \cdot 10^{-7}$
Balancing		μm		0.009	$\frac{2h_M}{(h_M - 2s_M)^2}n_{\text{g, air}}$		$3.8 \cdot 10^{-4}$
Contribution (in squared units)							
Correlated uncertainty component		$r_{\text{corr}}(x_i, x_j)$	$u_k(y) = 2c_i c_j u(x_i)u(x_j)r_{\text{corr}}(x_i, x_j)$				
Correlation between h_M and s_M			-0.14		$1.6 \cdot 10^{-9}$		
Standard uncertainty							
Calculated quantity		Function	Value	$u_c(y) = \left(\sum_i u_i^2(y) + \sum_k u_k(y)\right)^{1/2}$		Expanded uncertainty $U = 2u_c(y)$	
				Rand.	Sys.	Total	
Group refractive index of the sample	$n_{\text{g, sample}}$	$\frac{h_M}{h_M - 2s_M}n_{\text{g, air}}$	1.5426	$2.1 \cdot 10^{-3}$	$3.8 \cdot 10^{-4}$	$4.2 \cdot 10^{-3}$	

6.2 SPECTROMETER FDSCI LENGTH CALIBRATION

The length calibration of the spectrometer FDSCI setup using transparent plate transfer standards is the main result of paper I. In this paper, the refractive index of the transfer standards was quantified using a spectroscopic polarimeter (Horiba Jobin-Yvon, UVISEL-VASE). The calibration analysis presented here is augmented with the coverslip group refractive index results of paper II. In addition, systematic and random uncertainties are treated separately. The systematic uncertainty defines an uncertainty within which the true quantity value varies in a predictable manner in replicated measurements. In contrast, considering random uncertainty, the true quantity value varies in an unpredictable manner. The main source of systematic uncertainty is the calibration specimen of the scanning electron microscope that was used to specify the three coverslip transfer standards.

The measurement bias of the spectrometer FDSCI setup was calculated using an error function

$$e = h_M - h'_C = h_M - H_C n_g \left(1 + \frac{\theta_H^2}{2} \right) (1 + \alpha \Delta T), \quad (19)$$

where h'_C refers to calibrated optical thickness corrected for the cosine error. In our measurements, the measured optical thickness, h_M , and the calibrated geometric thickness, H_C , were quantified as the mean of five measurement points across the plate transfer standards. Random standard uncertainties for h_M and H_C , and the correlation between them, $r_{\text{corr}}(h_M, H_C)$, were obtained from the statistics of the five measurement points and from the uncertainty in each measurement. The uncertainty contribution associated with sample orientation in the h measurements was estimated as the maximum change in h_M as the sample was tilted across the acceptance angle of the system. In the H measurements, the uncertainty contribution associated with sample orientation was estimated using the cosine error in projection, Eq. (15). The thermal expansion between the h and H measurements was taken into account as $(1 + \alpha \Delta T)$, where ΔT is the temperature difference between the h and H measurement (ambient temperature). Because the temperatures were measured using the same thermometer, only the precision of the thermometer was considered. For the coverslip transfer standards, the linear coefficient of thermal expansion, α , was obtained from the datasheet of Schott D 263® M. A 10% common practice maximum variation was assumed for α . This was considered feasible, because the thermal expansion has small uncertainty contribution compared to other sources of uncertainty. The specification of the plastic transfer standards includes the thermal expansion within the temperature range $(21 \pm 2)^\circ\text{C}$. Table 2 shows the uncertainty budget calculated for the #00 coverslip transfer standard using correlated propagation of uncertainty [56].

Table 2. *Uncertainty budget for the #00 coverslip transfer standard. The total uncertainty was obtained as the root sum of squares from the random and systematic uncertainty components. The most important value is bolded.*

Uncertainty component	Unit	Value	Standard uncertainty		Sensitivity coefficient $c_i = \frac{\partial f}{\partial x_i}$	Contribution		
			$u(x_i)$			$u_i(y) = c_i u(x_i)$ [μm]		
			Rand.	Sys.		Rand.	Sys.	
Measured optical thickness	h_M	μm	110.01	0.14	1	0.14		
Sample orientation in h						0.29		
Calibrated geometric thickness	H_C	μm	71.49	0.07	0.41	$-n_g(1 + \theta_H^2/2)(1 + \alpha\Delta T)$	0.11	0.64
Sample orientation in H	θ_H	mrad	1.7	1.0		$-H_C n_g \theta_H (1 + \alpha\Delta T)$	$1.9 \cdot 10^{-4}$	
Group refractive index	n_g	-	1.5430	0.0016	0.0003	$-H_C(1 + \theta_H^2/2)(1 + \alpha\Delta T)$	0.11	0.02
Coefficient of thermal expansion	α	10^{-6} K^{-1}	7.2	0.4		$-H_C n_g(1 + \theta_H^2/2)\Delta T$	$2.8 \cdot 10^{-5}$	
Temperature between h and H	ΔT	°C	-0.60	0.16		$-H_C n_g(1 + \theta_H^2/2)\alpha$	$1.3 \cdot 10^{-4}$	
Correlated uncertainty component	$r_{\text{corr}}(x_i, x_j)$				Contribution			
					$u_k(y) = 2c_i c_j u(x_i) u(x_j) r_{\text{corr}}(x_i, x_j)$ [μm ²]			
					Rand.	Sys.		
Correlation between h_M and H_C		0.31			-0.010			
Calculated quantity	Function		Value [μm]	Standard uncertainty		Expanded uncertainty		
				$u_c(y) = \left(\sum_i u_i^2(y) + \sum_k u_k(y) \right)^{1/2}$		$U = 2u_c(y)$		
				[μm]		[μm]		
				Rand.	Sys.	Total		
Measured optical thickness	h_M		110.01	0.32		0.64		
Cosine error corrected and calibrated optical thickness	h'_C	$H_C n_g(1 + \theta_H^2/2)(1 + \alpha\Delta T)$	110.31	0.16	0.64	1.31		
Bias	e	$h_M - h'_C$	-0.30	0.34	0.64	1.45		

Figure 16 shows the measurement bias that corresponds to the five plate transfer standards. For clarity, the h'_C versus h_M –graph is shown as an inset. To correct for measurement bias, the calibration function, $C = ar$, was fitted to the measurement bias data using a weighted least squares algorithm. The calibration constant was quantified: $a = 0.000 \pm (0.002 + 0.012)$, where the first uncertainty represents random uncertainty, whereas the second uncertainty represents systematic uncertainty. Both uncertainties are quoted at a 95% confidence level. The zero value of a means that the factory calibration of the wavelength axis of the spectrometer (Ocean Optics, HR2000+) was valid. At a 95% confidence level, the random and systematic uncertainty of C equal $0.002r$ and $0.012r$, respectively, whereas in total, as

the root sum of squares, the uncertainty of C equals $0.012r$. In Fig. 16, the solid line represents C , whereas the dashed lines show the total uncertainty of C at a 95% confidence level.

All calibration data points include C within the random uncertainty at a 95% confidence level, Fig. 16. This implies that no significant length nonlinearity is present in the setup. The experimental data verifies the theoretical justification of the linear calibration function, $C = ar$.

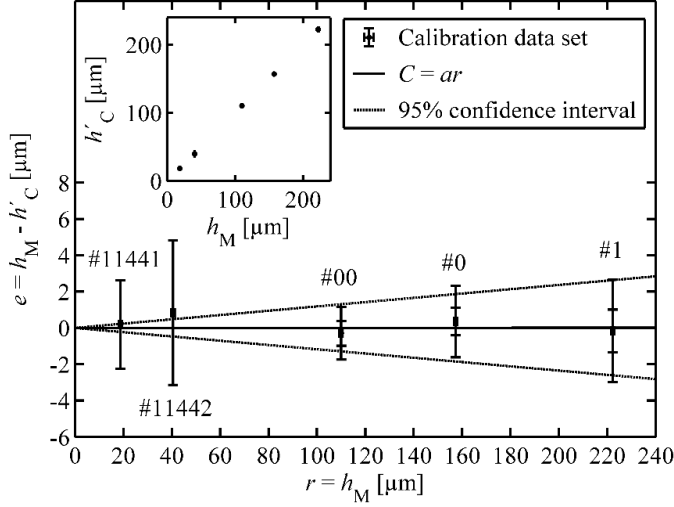


Figure 16 Measurement bias of the spectrometer FDSCI setup corresponding to five plate transfer standards. Error bars represent uncertainties at a 95% confidence level. For #00, #0, and #1 plate transfer standards, both random (lower error bar) and total uncertainty (higher error bar) are shown. Inset: h'_C versus h_M . Abbreviations: e , measurement bias; h_M , measured optical thickness; h'_C , cosine error corrected and calibrated optical thickness; r , optical length; C , calibration function; a , calibration constant.

6.3 STEP HEIGHT QUANTIFICATION ON COPPER DISC

Proof of concept of the Fourier domain short coherence interferometry (FDSCI) to verify the alignment of the accelerator discs of the Compact Linear Collider (CLIC) was shown in Paper III. In this paper a calibrated spectrometer FDSCI was employed to determine the height of two steps, machined on a copper disc according to the CLIC manufacturing tolerances [1]. The presented results here were obtained using the spectrometer FDSCI length calibration result of section 6.2.

An oxygen-free electronic copper disc (diam. = 40 mm) with 0, 50, 110, and 150 μm nominal ultraprecisely turned levels (surface roughness, $R_a \leq 25 \text{ nm}$, flatness $\leq 2 \mu\text{m}$) was used as a step sample, Fig. 17. 50, 110, and 150 μm levels formed 40 and 60 μm tall steps.

The three-dimensional (3D) profile of the copper step sample was reconstructed by scanning the probe beam across the sample, with 0.1 mm translation increments at an azimuth angle between 0° to 165° , in 15° steps, Fig. 18(a). At each lateral position, the FDSCI measurement was repeated 10 times. The scanning was performed from left to right and back. To obtain a calibrated geometric step profile, the measured optical lengths, r_M , were: 1) calibrated by Eq. (18), using the calibration result of section 6.2, 2) transformed using the group refractive index of the ambient air, $n_{g, \text{air}}$, and 3) corrected for thermal expansion in comparison to a standard temperature of $T_s = 20^\circ\text{C}$.

$$R_{CM} = \frac{r_{CM}}{n_{g, \text{air}}} (1 + \alpha \Delta T) \quad (20)$$

Here, r_{CM} and R_{CM} refer to the calibrated measured optical and geometric length, respectively. The uncertainty contribution associated with sample orientation was estimated to equal that in the calibration measurements. The thermal expansion was taken into account as $(1 + \alpha \Delta T)$, where the temperature difference is between the standard and the measurement temperature, $\Delta T = T_s - T_M$. For oxygen-free electronic copper alloys [57], the linear coefficient of thermal expansion, α , equals $(16.9 \pm 1.0) \cdot 10^{-6}/\text{K}$ with 10% common practice maximum variation assumed. Table 3 shows an example of the uncertainty budget calculated for R_{CM} at a point 16.5 mm in the 0° azimuth angle right scan of the copper step sample, using uncorrelated propagation of uncertainties [56]. This measurement point is indicated in Fig. 18(b) by a blue arrow. Even though the input quantities may correlate, the correlated uncertainty contributions are negligible because of the dominant uncertainty contributions from r_{CM} and sample orientation. Consequently, an uncorrelated analysis was applied. The systematic uncertainties from point-to-point were treated separately from the random uncertainties.

Results

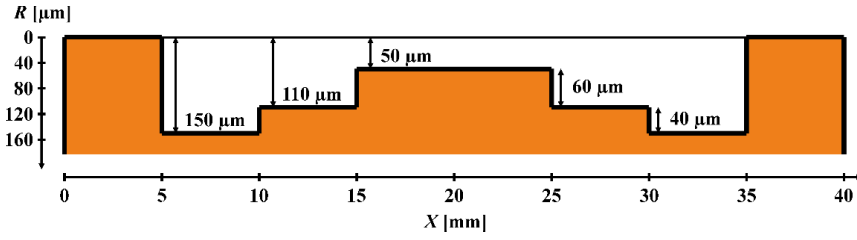


Figure 17 Nominal cross-sectional geometry of turned copper step sample.

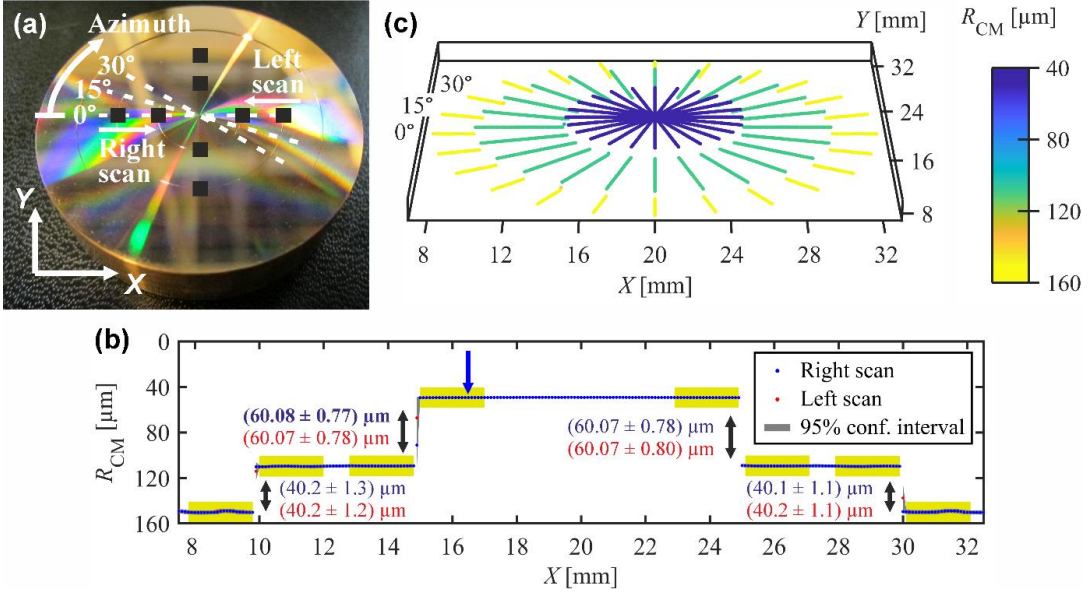


Figure 18 Three-dimensional (3D) measurement result of the copper step sample, with the coordinate system the same as in Fig. 17. (a) Photograph of copper step sample, with dashed white lines indicating the path of the spectrometer FDSCI scanning, whereas black squares indicate areas measured with the Veeco-NT3300. (b) Spectrometer FDSCI step profile at 0° azimuth angle. Scanning was performed from left to right and back, the right scan shown on top of the left scan. Blue arrow at 16.5 mm indicates the measurement point for which the example R_{CM} uncertainty budget is calculated. Step heights are determined from the yellow boxed regions of interest (ROI) by subtracting the upper level from the lower level. The upper step heights correspond to the right scan, whereas the lower step heights correspond to the left scan. Uncertainties are quoted at 95% confidence level. The example step height uncertainty budget is calculated for the bolded result of step at 15 mm. (c) 3D profile of the copper step sample measured using the spectrometer FDSCI. Abbreviations: R_{CM} , calibrated measured geometric length; X and Y, lateral coordinates across the sample.

Figure 18(b) shows an example step profile scanned at 0° azimuth angle and plotted in the same coordinate system as in Fig. 17. The scanned profiles were leveled to the $150\ \mu\text{m}$ level by fitting a line to the $150\ \mu\text{m}$ level measurement data and by setting this level to the $150\ \mu\text{m}$ value. The blue and red dots represent the measured profile, whereas the gray belt represents the uncertainty of the profile at a 95% confidence level. The step heights, H_{step} ,

were analyzed inside the yellow boxed regions of interest (ROI, 2 mm wide) of the step profile, Fig. 18(b), by subtracting the upper ROI mean from the lower ROI mean. The uncertainty of the step height was evaluated using correlated propagation of uncertainty [56]. The measured step profiles exhibit systematic uncertainty from point to point because of the common calibration and common $n_{g, \text{air}}$ and thermal expansion estimation, Table 3. From point to point, this systematic uncertainty correlates with a correlation coefficient of 1. The random uncertainty of the upper and lower ROI mean includes the random uncertainty at each measurement point inside ROI and the maximum deviation of the profile inside ROI. Table 4 shows an example step height uncertainty budget calculated for a step at 15 mm in the 0° azimuth angle for the scan moving to the right. An example step height is indicated in Fig. 18(b) as a bolded result. In all step height measurement the uncertainty at 95% confidence level was less than $2.2 \mu\text{m}$. Figure 18(c) shows the 3D profile of the copper step sample.

Table 3. *Uncertainty budget for the calibrated measured geometric length at point 16.5 mm in the 0° azimuth angle right scan of the copper step sample. The total uncertainty was obtained as root sum of squares from the random and systematic uncertainty components. The most important value is bolded.*

Uncertainty component	Unit	Value	Standard uncertainty		Sensitivity coefficient $c_i = \frac{\partial f}{\partial x_i}$	Contribution	
			$u(x_i)$			$u_i(y) = c_i u(x_i)$ [μm]	
			Rand.	Sys.		Rand.	Sys.
Calibrated measured optical length	r_{CM} μm	51.55	0.01	0.30	$\frac{1}{n_{\text{g, air}}}(1 + \alpha\Delta T)$	0.01	0.30
Sample orientation						0.29	
Group refractive index of air	$n_{\text{g, air}}$ -	1.00027394	$0.2 \cdot 10^{-7}$	$5.3 \cdot 10^{-7}$	$-\frac{r_{\text{CM}}}{n_{\text{g, air}}^2}(1 + \alpha\Delta T)$	$1.2 \cdot 10^{-6}$	$2.7 \cdot 10^{-5}$
Coefficient of thermal expansion	α 10^{-6}K^{-1}	16.9		1.0	$\frac{r_{\text{CM}}}{n_{\text{g, air}}}\Delta T$		$1.3 \cdot 10^{-4}$
Temperature difference	ΔT $^{\circ}\text{C}$	-2.57	0.01	0.58	$\frac{r_{\text{CM}}}{n_{\text{g, air}}}\alpha$	$5.8 \cdot 10^{-6}$	$5.0 \cdot 10^{-4}$
Calculated quantity	Function	Value [μm]	Standard uncertainty		$u_c(y) = \left(\sum_i u_i^2(y)\right)^{1/2}$ [μm]	Expanded uncertainty	
						$U = 2u_c(y)$ [μm]	
					Rand.	Sys.	Total
Calibrated measured geometric length	R_{CM} $\frac{r_{\text{CM}}}{n_{\text{g, air}}}(1 + \alpha\Delta T)$	51.54		0.29		0.30	0.83

Step heights quantified for the two steps were: $(40.27 \pm 0.50) \mu\text{m}$ ($N = 48$) and $(60.05 \pm 0.71) \mu\text{m}$ ($N = 48$). To verify the spectrometer FDSCI profiling, the copper step sample was also measured using a Veeco-NT3300 white light interferometer, $20\times$ magnification, and $298 \mu\text{m} \times 226 \mu\text{m}$ field of view. The measurement areas are shown in Fig. 18(a) as black squares. The results

of the validating measurement were: $(40.27 \pm 0.14) \mu\text{m}$ ($N = 4$) and $(60.44 \pm 0.22) \mu\text{m}$ ($N = 4$). All uncertainties quoted at 95% confidence level. The two step height measurements show overlapping results, which verifies the validity of spectrometer FDSCI profiling.

Table 4. Step height uncertainty budget for a step at 15 mm in the 0° azimuth angle right scan of the copper step sample. The scan was leveled to the $150 \mu\text{m}$ level. The total uncertainty was obtained as the root sum of squares from the random and systematic uncertainty components. The most important value is bolded.

				Sensitivity coefficient				
Uncertainty component		Unit	Value	Standard uncertainty		$c_i = \frac{\partial f}{\partial x_i}$	Contribution	
				$u(x_i)$			$u_i(y) = c_i u(x_i)$ [μm]	
				Rand.	Sys.		Rand.	Sys.
Upper region of interest mean	ROI _{upper}	μm	49.42	0.08	0.30	1	0.08	0.30
Lower region of interest mean	ROI _{lower}	μm	109.50	0.12	0.66	-1	0.12	0.66
Correlated uncertainty component				Contribution				
			$r_{\text{corr}}(x_i, x_j)$	$u_k(y) = 2c_i c_j u(x_i) u(x_j) r_{\text{corr}}(x_i, x_j)$ [μm ²]				
							Rand.	Sys.
Systematic uncertainty in ROI _{upper} and ROI _{lower}			1					-0.40
				Standard uncertainty			Expanded uncertainty	
Calculated quantity		Function	Value [μm]	$u_c(y) = \left(\sum_i u_i^2(y) + \sum_k u_k(y) \right)^{1/2}$			$U = 2u_c(y)$	
				[μm]			[μm]	
				Rand.	Sys.	Total		
Step height	H_{step}	$H_{\text{step}} = \text{ROI}_{\text{lower}} - \text{ROI}_{\text{upper}}$	60.08	0.15	0.35	0.77		

The uncertainty of the average result is smaller than the uncertainty of a single step height measurement. This is due to the fact that the uncertainty propagates in mean as

$$\sqrt{\left(\frac{s(x_i)}{\sqrt{N}}\right)^2 + \left(\frac{1}{N} \sqrt{\sum_{i=1}^N u_{\text{rand}}^2(x_i)}\right)^2 + \left(\frac{\sum_{i=1}^N u_{\text{sys}}(x_i)}{N}\right)^2}, \quad (21)$$

where $s(x_i)$ is the standard deviation of N times repeated measurements x_i . Moreover, $u_{\text{rand}}(x_i)$ and $u_{\text{sys}}(x_i)$ are the random and systematic uncertainty, respectively, of the individual measurements. The first term accounts for the standard uncertainty of the mean, whereas the second and third terms account for the random and systematic uncertainty, respectively, in each measurement. As N increases, the first and second term decrease, whereas the third term stays constant (if $u_{\text{sys}}(x_i)$ are identical). Therefore, the total uncertainty of repeated measurement approaches the systematic uncertainty of the measurement, as expected.

6.4 QUALITATIVE AS-DISC INTERNAL MEASUREMENT

Currently unpublished qualitative results of an internal measurement of one accelerating structure (AS) disc are presented next. The most important result is that the fiber-optic FDSCI can measure the profile of the hard-to-reach internal structure of the AS-disc.

Figure 19(a) shows a mock-up AS-disc under measurement. The mock-up disc has a 45 mm outer diameter, 9.73 mm cavity radius, 4.70 mm iris diameter, and 10.34 mm height. The 3.85 mm diameter fiber-optic probe was inserted through the AS-cavity and oriented to maximize the interference amplitude. A vertical, Z , profile of the mock-up disc was reconstructed by pulling back the probe across the disc with 50 μm translation increments at the iris region and with 200 μm increments at the cavity wall region. The scan was performed along the “up” and “down” directions. At each position, the FDSCI measurement was repeated 10 times. Figure 19(b) shows the measured vertical profile and A-scans for the iris and for the cavity wall regions in the up direction scan. Measurement points for the A-scans are indicated by blue arrows. Prior to length calibration, the measured optical lengths are shown as an index without length unit. The linear k -space resampling was done with the resampling parameters of the $Z = 0.4$ mm measurement point.

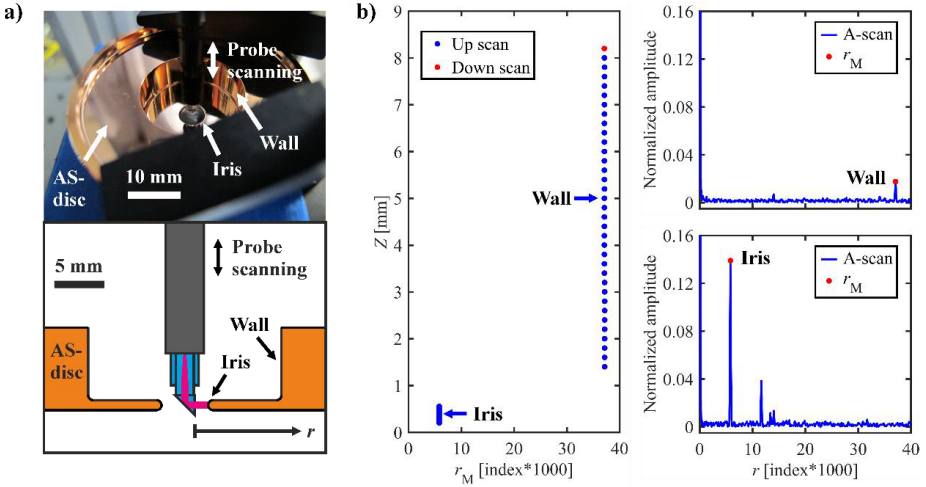


Figure 19 (a) Measurement of a mock-up of the accelerating structure (AS) disc using the fiber-optic FDSCI setup, with photograph (top) and measurement schematics (bottom). (b) Vertical profile of the mock-up AS-disc. Scanning was performed by moving the fiber-optic probe up and down, the up scan shown on top of the down scan. A-scans for the iris (bottom) and for the cavity wall (top) regions in the up scan are shown on the right. Blue arrows indicate the measurement points in the A-scans. Prior to length calibration, the measured optical lengths are shown as an index without length unit. r , optical length; r_M , measured optical length; Z , vertical coordinate across the AS-disc.

7 DISCUSSION

We applied a calibrated spectrometer FDSCI to quantify the profile and step heights of an ultraprecisely machined copper step sample. The experiment demonstrated proof of concept of using Fourier domain short coherence interferometry (FDSCI) as a means to quantify the internal alignment and shape of the accelerating structures of the Compact Linear Collider (CLIC). The proof is based on two steps: First, the described length calibration and accuracy evaluation apply, because both the spectrometer and the fiber-optic FDSCI employ the introduced common-path technique. Second, the step height measurement on the copper step sample showed submicron accurate shape profiling relevant to quantification of typical accelerating structure (AS) disc stack shape errors, depicted in Fig. 2.

7.1 RELEVANCE OF THE RESULTS TOWARDS SUBMICRON ACCURATE FIBER-OPTIC FDSCI

In section 4.2, it was suggested that the fiber-optic FDSCI setup be improved by a pre-calibration procedure in order to stabilize the A-scans. To achieve this in parallel with the AS measurement, we added a pre-calibration unit to the fiber-optic FDSCI setup via a fiber coupler. Figure 20 shows the upgraded setup schematics. In this unit, common-path interference signals from a fixed air gap are recorded. The interference signal in air provides the linear k -space resampling, while the nominal gap length (e.g. 15 mm) precalibrates the A-scans. The primary length calibration of the fiber-optic FDSCI is conducted in a separate Sagnac type interferometer using 0.1 – 10 mm thick fused silica transfer standards and following the approach described in sections 6.1 and 6.2. This procedure transfers the calibration obtained by the fused silica standards into the fixed air gap. As the fiber-optic probe inserted into the AS-cavity operates in common-path configuration, no dispersion due to the optical fiber is added, see section 3, and the length calibration is thus successfully transferred into the AS measurement using Eq. (18). The nearly nondispersive medium in the fixed gap ensures that the length calibration is robust against variations in the system spectrum. Hence, the photodetectors in the upgraded setup, Fig. 20, do not have to be identical, and the pass band sweep of the fiber Fabry-Perot spectral filter (FFP) may drift without losing the calibration.

To exploit the full measurement range and axial resolution that the FFP provides, we replace the low power light emitting diode with a swept laser source [58]. This ring cavity light source comprises the FFP, a semiconductor optical amplifier (SOA) as gain medium, isolators, and a fiber coupler to extract light from the ring cavity, Fig. 20. The lasing builds up from

spontaneous emission in the SOA as light circulates in the cavity. The output light power is ca 0.1 mW [58]. This approach provides orders of magnitude more light power on the photodetectors, compared to the setup presented in section 4.2.

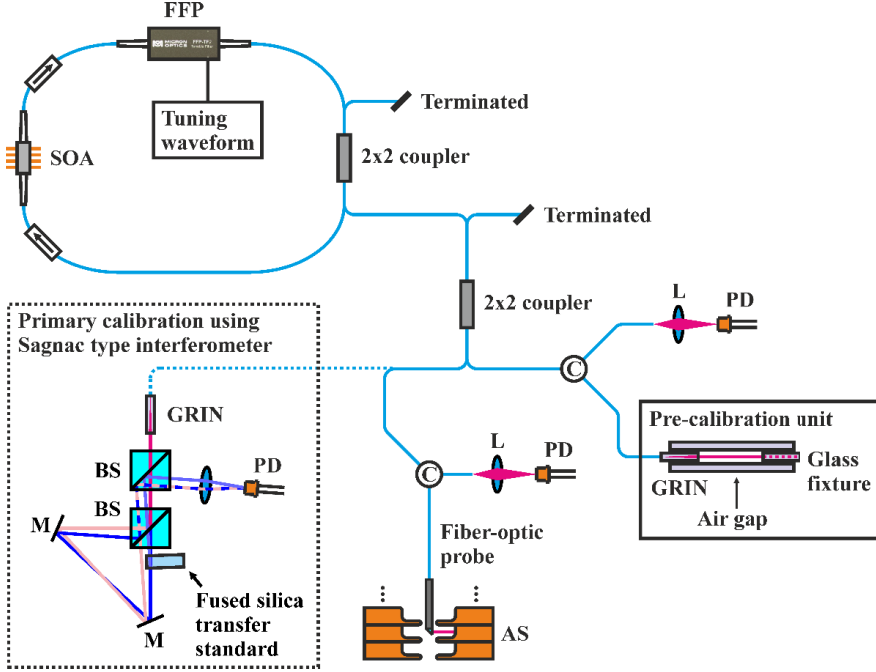


Figure 20 Fiber-optic FDSCI upgrade schematics. The upgraded setup features a pre-calibration unit with a fixed air gap and a swept laser light source. The interference signal from the air gap provides linear k -space resampling, while the nominal gap length pre-calibrates the recorded A-scans in the system. The primary length calibration is conducted in a separate Sagnac type interferometer by fused silica transfer standards. Abbreviations: SOA, semiconductor optical amplifier; FFP, fiber Fabry-Perot spectral filter; GRIN, gradient index lens; C, optical circulator; BS, beam splitter; M, mirror; L, lens; PD, photodetector; AS, accelerating structure.

The reported measurement accuracy holds within a measurement range of 240 μm . Therefore, the effect of extending the range to 10 mm on the measurement accuracy needs to be discussed. The measurement accuracy at 10 mm could be estimated by employing the sensitivity coefficients of the uncertainty sources of the calibrated measured geometric length, R_{CM} (Table 3). Air group refractive index ($n_{\text{g, air}}$) and thermal expansion (α , and ΔT) uncertainty components have 100 times increased uncertainty contributions because their sensitivity coefficients, c , depend on the optical length, r_{CM} . At 10 mm these uncertainty components nonetheless contribute less than 0.1 μm uncertainty. The introduced way of handling uncertainty contribution associated with sample orientation includes cosine and wavefront errors in the system. At 10 mm and with 3.0 mrad acceptance

angle, the cosine error, Eq. (13), contributes on the order of $0.01 \mu\text{m}$. The wavefront error is a characteristic of the system. However, the acceptance angle of the fiber-optic FDSCI (3.0 mrad) is approximately the same as in the Sagnac type FDSCI ($0.2^\circ \approx 3.5 \text{ mrad}$) and therefore, an uncertainty contribution on the order of $0.1 \mu\text{m}$ is expected to be associated with sample orientation. The pre-calibration ensures better than $0.2 \mu\text{m}$ repeatability. In the primary calibration, the accuracy of the geometric thickness should be on the order of $0.1 \mu\text{m}$. Table 2 indicates that the sensitivity, c , attributed to the transfer standards' group refractive index, n_g , uncertainty is directly proportional to the geometric thickness, Hc . However, thick transfer standards do not cause increased uncertainty contribution, because the quantification of n_g gets more accurate with increasing sample thickness. The latter is evident from Table 1, where the sensitivities, c , attributed to the measured quantities (optical thickness, h_M , and Sagnac beam path difference, s_M) decrease with increasing sample thickness: The denominator increases quadratically, while the nominator increases linearly.

According to the above considerations, the upgraded fiber-optic FDSCI is expected to provide submicron accurate absolute length measurement across a 10 mm measurement range.

7.2 CLIC-AS INTERNAL ALIGNMENT MEASUREMENT STRATEGY

The next step is to measure a complete accelerating structure (AS) disc stack. To do this, the fiber-optic FDSCI setup should be integrated into a cylindrical scanning device that provides disc stack rotation and pullback of the fiber-optic probe from the AS-cavity. This gives a point cloud in cylindrical coordinates: The FDSCI provides the radial, R , coordinate whereas the vertical, Z , and angular, γ , coordinates are obtained from the pullback and rotation stage encoders. The scanning will cause similar image distortions, as seen in intravascular ultrasound imaging [59, 60], due to the eccentricity of the disc stack with respect to the rotation axis, and due to nonparallel pullback relative to the rotation axis. To minimize image distortions, we propose a measurement strategy, as follows, to quantify typical AS-cavity shape errors depicted in Fig. 2.

1) AS-disc stack alignment measurement (Fig. 2, Type 1 shape error)

The eccentricity of the disc stack with respect to the rotation axis causes the circular shape of irises to appear distorted. Using a narrow acceptance angle fiber-optic probe, the point cloud of an eccentric iris appears discontinued, as no light is gathered at incidence angles above the acceptance angle, and distorted because of the generated cosine error within the acceptance angle. Therefore, any quantification of the geometric center of the iris by using a circular fit will give an erroneous

result. However, at two angular scan coordinates, the iris is perpendicular to the optical axis, and the R coordinate is thus uncorrupted. From the point cloud, these two angles can be identified as local DC peak intensity maxima. Figure 21 depicts the measurement geometry. From this data the eccentricity, E_{rot} , of the geometric center of the iris with respect to the rotation axis is calculated as

$$E_{\text{rot}} = \frac{R_1 - R_2}{2 \sin\left(\frac{\gamma_2 - \gamma_1}{2}\right)}. \quad (22)$$

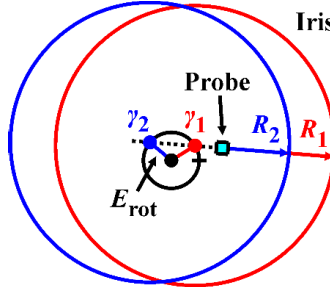


Figure 21 Rotational eccentricity measurement. Red and blue circles represent the iris at two rotation angle coordinates. Abbreviations: R , radial coordinate; γ , angular coordinate; E_{rot} , rotational eccentricity of the geometric center of the iris (red and blue dot) with respect to the rotation axis (black dot).

Calculating the rotational eccentricity of each iris gives the alignment of the AS-disc stack. First, the zenith position of an iris is found by the Z -scan, and second, the eccentricity measurement is done by the angular scan. Third, the eccentricity measurement is repeated for each iris in the AS-disc stack. The result is plotted in a cylindrical coordinate system of $(Z, \gamma_1, E_{\text{rot}})$, and the alignment is analyzed as maximum deviation from the centerline in μm .

This method of measuring the rotational eccentricity is invariant in the position of the fiber-optic probe with respect to the rotation axis, as long as the extension of the optical axis, Fig. 21 (dashed line), intersects the circle drawn by E_{rot} . Hence, nonparallelism of the pullback axis with respect to the rotation axis does not affect the alignment measurement. The rotary table has characteristic radial error motion and tilt error motion [61]. At a 300 mm height above the rotary table, ball bearing based systems typically introduce a few micrometer uncertainty contribution to the measured R coordinate. In air bearing systems, this uncertainty contribution is on the order of $0.1 \mu\text{m}$. Tilt shift of the irises due to the rotor alignment and disc stack placing on the rotor causes less than $0.01 \mu\text{m}$ error in $R_1 - R_2$ in Eq. (22). This approximately corresponds to a situation where a human hair is left under the disc stack. Angular coordinates of perpendicular iris orientation with respect

to the optical axis, γ_1 and γ_2 , were determined as local DC peak intensity maxima. The angular uncertainty is thus determined by the uncertainty of the DC peak intensity. In 100 A-scan repeats, this corresponds to less than 0.1° angular uncertainty. The sensitivity of E_{rot} to the uncertainty of the half of the angular difference, $\Delta\gamma/2 = (\gamma_2 - \gamma_1)/2$, is

$$\frac{\partial E_{\text{rot}}}{\partial \left(\frac{\Delta\gamma}{2}\right)} = \frac{(R_1 - R_2) \cos\left(\frac{\Delta\gamma}{2}\right)}{\cos(\Delta\gamma) - 1}. \quad (23)$$

Equation (23) reveals that at $\Delta\gamma = 180^\circ$, the situation where the rotation axis coincides with the extension of the optical axis, compare Fig. 21, the sensitivity of E_{rot} to the angular uncertainty is zero. Hence, the contribution of the angular uncertainty to E_{rot} is also zero. However, this assumption is impractical, as no perfect probe positioning can be achieved. At small angle deviation, $\gamma_1 < 10^\circ$ and $\gamma_2 > 170^\circ$, and by assuming $R_1 - R_2 = 100 \mu\text{m}$ and 2.35 mm iris radius, the uncertainty contributions of the angular uncertainty and correlation between R and γ are $< 0.01 \mu\text{m}$. The length difference, $R_1 - R_2$, resembles the step height measurement. In this differential measure, the uncertainty contribution from the calibration is $< 0.01 \mu\text{m}$, due to systematics, i.e., the calibration is common for R_1 and R_2 . For E_{rot} , the above considerations indicate that the dominant uncertainty contributions arise from the repeatability of the FDSCI, from sample orientation, and from the radial error motion of the rotary table. In total, we expect to quantify E_{rot} of the discs with micron accuracy. Hence, the fiber-optic FDSCI can quantify whether the discs are bonded to better than $5 \mu\text{m}$ alignment.

2) Internal shape measurement of AS-disc stack with rotational eccentricity correction and outer surface referencing

To measure the internal shape of the AS-disc stack with minimized rotational eccentricity induced distortion, we apply a second set of measurements. These measurements employ rotational eccentricity zeroing and perform probe repositioning for each iris. The rotational eccentricity zeroing is done by translating the disc stack on the rotary table based on the measured E_{rot} values in part 1. Repositioning of the probe is done by translating the probe along the tangential direction (perpendicular to R) to maximize the DC level of the signal at each iris. The effect of residual rotational eccentricity and probe positioning error in pullback across a disc is included in the uncertainty associated with sample orientation. In total, the tolerance for the residual alignment errors is $7 \mu\text{m}$ at iris and $25 \mu\text{m}$ at wall regions, with the 3.0 mrad acceptance angle fiber-optic probe.

To fix the internal measurement to the external surface of the AS-disc stack, we propose to add a second fiber-optic probe to be able

to concurrently measure the internal, R_I , and external, R_E , surface of the AS-disc stack, Fig 22(a). The two probes are coupled to each other in a Sagnac configuration, and the coaxiality of the two probe beams is ensured to better than 1 mrad by applying the Sagnac interferometer balancing procedure. The interprobe distance, D (~ 50 mm), could be calibrated by measuring the surface positions of a length transfer standard of known thickness, H , Fig. 22(b). In this way, the wall thickness, W , is measured with micron accuracy. As R_I and R_E compensate each other, the radial error motion of the rotary table and waviness conical image distortion caused by nonparallel and nonflat pullback relative to the rotation axis do not affect the measured W . In the measurement configuration of two opposing light beams, the phase shifts related to the reflection phenomena do not cancel, and a correction of ca. 50 nm is required in W at a 1550 nm wavelength.

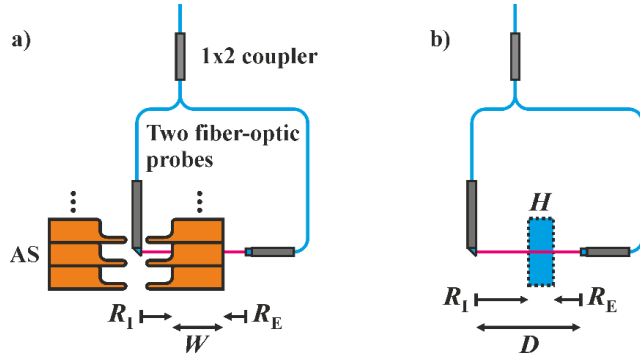


Figure 22 (a) Concurrent internal, R_I , and external, R_E , measurement to quantify wall thickness, W , of the accelerating structure (AS). (b) The coaxial alignment of the two beams is ensured by maximizing the interference intensity in the Sagnac type interferometer formed by the two probes. The internal and external measurements are fixed to each other by calibrating the interprobe distance, D . This linkage is obtained by use of a length transfer standard of known thickness, H .

The accelerating structure (AS) measurement task is finalized by a coordinate measuring machine (CMM) inspection on the external surface of the disc stack. CMM and the Fourier domain short coherence interferometry (FDSCI) measurements are stitched to each other using the external reference system of the AS (eight reference spheres mounted on the AS-disc stack). In the R direction, the uncertainty of the CMM referenced internal shape comprises probing error [4, 62] contribution of the CMM and the W uncertainty contribution of the FDSCI. In total, 2 μm accuracy is expected. This does not fulfill the required tolerance of the AS-cavity diameter (Fig. 2, Type 2 shape error). However, if the AS-cavity diameter is analyzed from a wider field of view on the wall region, compare to the regions of interest (ROI) boxes in Fig. 18(b), the random uncertainty components will have

reduced contributions due to averaging. With this approach, submicron accuracy can be achieved.

The heavily rounded form of the iris in the Z direction is not seen in Fig. 19 because of the $500\text{ }\mu\text{m}$ beam diameter. Iris shapes could be analyzed from the measured point cloud by determining zenith positions on the iris. The zenith position at each angular coordinate can be identified as a local DC peak intensity maximum across the vertical coordinate. A second degree fit to (Z , DC peak intensity)-data determines the zenith positions, even with submicron precision, including contributions from the fitting uncertainty and from the axial error motion of the rotary table [61]. Thus, iris shape errors (Fig. 2, Type 3 shape error) can be identified within the required tolerance. Systematic tilt of discs (Fig. 2, Type 4 shape error) could be analyzed as orientation of irises with respect to the centerline of the disc stack. The orientation of irises is required to be quantified with better than $0.5\text{ }\mu\text{m}$ accuracy. This requirement stands on the limit of zenith position evaluation and could probably just be detected.

8 CONCLUSIONS

Even micrometer-level misalignments significantly reduce the performance of accelerating structures that are on the critical path towards successful operation of the Compact Linear Collider (CLIC). In this thesis, I showed a calibration procedure of a Fourier domain short coherence interferometer instrument intended for submicron accurate internal alignment quantification of the CLIC accelerating structures.

The presented length calibration relies on transparent plate transfer standards with certified geometric thickness. The group refractive index of the plate transfer standards, necessary to translate the certified geometric thickness into optical thickness, was quantified using a Sagnac type interferometer. The linear length calibration function characteristic of common-path Fourier domain interferometers allowed accurate group index evaluation, based on two uncalibrated length measures. This is an important property of the presented technique, as no other refractive index measurements or specifications are required on the transfer standards. Other sources of uncertainty included measurement repeatability, sample orientation, thermal expansion, and the group refractive index of air. The technique provided a calibration function with evaluated uncertainty. The presented length calibration technique is applicable in any Fourier domain optical coherence device, benefiting a broad field of optics.

A measurement on an ultraprecisely machined copper step sample provided proof of concept. In this experiment, submicron accurate shape profiling was achieved at a 95% confidence level on the exact same structures that are responsible in the internal alignment quantification of the CLIC accelerating structures. The fiber-optic setup provides access inside the hard-to-reach accelerator cavity and a measurement range that exceeds the 8.6 mm cavity radius.

In conclusion, fiber-optic Fourier domain short coherence interferometer shows promise as a quality assurance tool to determine whether the accelerating structures are assembled to stringent tolerances.

REFERENCES

1. A Multi-TeV linear collider based on CLIC technology: CLIC Conceptual Design Report, edited by M. Aicheler, P. Burrows, M. Draper, T. Garvey, P. Lebrun, K. Peach, N. Phinney, H. Schmickler, D. Schulte and N. Toge, CERN-2012-007, pp. 1–5 and 345–417.
2. J. Wang, J. Lewandowski, J. V. Pelt, C. Yoneda, G. Riddone, D. Gudkov, T. Higo and T. Takatomi, "Fabrication technologies of the high gradient accelerator structures at 100MV/m range," in *The 1st International Particle Accelerator Conference*, Kyoto, Japan, JACoW, THPEA064 (2010).
3. R. Zennaro, "Study of the machining and assembly tolerances for the CLIC accelerating structures," EUROTeV-Report-2008-081, http://www.eurotev.org/reports_presentations/eurotev_reports/2008/e1532/EUROTeV-Report-2008-081.pdf (Accessed 4 February 2018).
4. S. Atieh, M. Aicheler, G. Arnau-Izquierdo, A. Cherif, L. Deparis, D. Glaude, L. Remandent, G. Riddone, M. Scheubel, D. Gudkov, A. Samoshkin and A. Solodko, "Machining and characterizing X-band RF-structures for CLIC," in *The 2nd International Particle Accelerator Conference*, San Sebastián, Spain, JACoW, TUPS098 (2011).
5. S. O. Kasap, *Optoelectronics and Photonics: Principles and Practices*, 2nd edn. (Pearson Education Limited, Essex, England, 2013), pp. 135–142 and 381–395.
6. J. A. Izatt and M. A. Choma, "Theory of Optical Coherence Tomography," in *Optical Coherence Tomography: Technology and Applications*, W. Drexler and J. G. Fujimoto (Eds.), (Springer, Berlin Heidelberg New York, 2008), pp. 47–72.
7. A. Bers, "Note on group velocity and energy propagation," *American Journal of Physics* **68**(5), 482–484 (2000).
8. K. Tan, M. Mazilu, T. Chow, W. Lee, K. Taguchi, B. Ng, W. Sibbett, C. Herrington, C. Brown and K. Dholakia, "In-fiber common-path optical coherence tomography using a conical-tip fiber," *Optics Express* **17**(4), 2375–2384 (2009).
9. A. B. Vakhtin, D. J. Kane, W. R. Wood and K. A. Peterson, "Common-path interferometer for frequency-domain optical coherence tomography," *Applied Optics* **42**(34), 6953–6958 (2003).
10. E. Hecht, *Optics*, 5th edn. (Pearson Education Limited, Essex, England, 2017), pp. 121–133.
11. P. de Groot, X. C. de Lega, J. Kramer and M. Turzhitsky, "Determination of fringe order in white-light interference microscopy," *Applied Optics* **41**(22), 4571–4578 (2002).

12. A. Dubois, J. Selb, L. Vabre and A.-C. Boccard, "Phase measurements with wide-aperture interferometers," *Applied Optics* **39**(14), 2326–2331 (2000).
13. K. Creath, "Calibration of numerical aperture effects in interferometric microscope objectives," *Applied Optics* **28**(16), 3333–3338 (1989).
14. C. Baylard, A. A. Maradudin and J.-J. Greffet, "Coherent reflection factor of a random rough surface: applications," *Journal of the Optical Society of America A* **10**(12), 2637–2647 (1993).
15. J. Caron, J. Lafait and C. Andraud, "Scalar Kirchhoff's model for light scattering from dielectric random rough surfaces," *Optics Communications* **207**(1), 17–28 (2002).
16. J. Sánchez-Gil, E. Méndez and A. Maradudin, "Limits of validity of three perturbation theories of the specular scattering of light from one-dimensional, randomly rough, dielectric surfaces," *Journal of the Optical Society of America A* **12**(7), 1547–1558 (1995).
17. H. Bennett and J. Porteus, "Relation between surface roughness and specular reflectance at normal incidence," *Journal of the Optical Society of America* **51**(2), 123–129 (1961).
18. J. Porteus, "Relation between the height distribution of a rough surface and the reflectance at normal incidence," *Journal of the Optical Society of America* **53**(12), 1394–1402 (1963).
19. M. Bjuggren, L. Krummenacher and L. Mattsson, "Noncontact surface roughness measurement of engineering surfaces by total integrated infrared scattering," *Precision Engineering* **20**(1), 33–45 (1997).
20. I. Grulkowski, J. J. Liu, B. Potsaid, V. Jayaraman, J. Jiang, J. G. Fujimoto and A. E. Cable, "High-precision, high-accuracy ultralong-range swept-source optical coherence tomography using vertical cavity surface emitting laser light source," *Optics Letters* **38**(5), 673–675 (2013).
21. M. Gora, K. Karnowski, M. Szkulmowski, B. J. Kaluzny, R. Huber, A. Kowalczyk and M. Wojtkowski, "Ultra high-speed swept source OCT imaging of the anterior segment of human eye at 200 kHz with adjustable imaging range," *Optics Express* **17**(17), 14880–14894 (2009).
22. I. Grulkowski, J. J. Liu, B. Potsaid, V. Jayaraman, C. D. Lu, J. Jiang, A. E. Cable, J. S. Duker and J. G. Fujimoto, "Retinal, anterior segment and full eye imaging using ultrahigh speed swept source OCT with vertical-cavity surface emitting lasers," *Biomedical Optics Express* **3**(11), 2733–2751 (2012).
23. M. J. Gora, J. S. Sauk, R. W. Carruth, K. A. Gallagher, M. J. Suter, N. S. Nishioka, L. E. Kava, M. Rosenberg, B. E. Bouma and G. J. Tearney, "Tethered capsule endomicroscopy enables less invasive imaging of gastrointestinal tract microstructure," *Nature Medicine* **19**(2), 238–240 (2013).

24. J. Mavadia, J. Xi, Y. Chen and X. Li, "An all-fiber-optic endoscopy platform for simultaneous OCT and fluorescence imaging," *Biomedical Optics Express* **3**(11), 2851–2859 (2012).
25. Novacam Technologies Inc., "TubeInspect," <http://www.novacam.com/products/tube-inspect-for-tube-id-and-od/> (Accessed 6 February 2018).
26. J. Binding, J. Ben Arous, J.-F. Léger, S. Gigan, C. Boccara and L. Bourdieu, "Brain refractive index measured in vivo with high-NA defocus-corrected full-field OCT and consequences for two-photon microscopy," *Optics Express* **19**(6), 4833–4847 (2011).
27. N. Sandler, I. Kassamakov, H. Ehlers, N. Genina, T. Ylitalo and E. Haeggstrom, "Rapid interferometric imaging of printed drug laden multilayer structures," *Scientific Reports* **4**, 4020 (2014).
28. S. Yokoyama, J. Ohnishi, S. Iwasaki, K. Seta, H. Matsumoto and N. Suzuki, "Real-time and high-resolution absolute-distance measurement using a two-wavelength superheterodyne interferometer," *Measurement Science and Technology* **10**(12), 1233–1239 (1999).
29. P. de Groot, "Principles of interference microscopy for the measurement of surface topography," *Advances in Optics and Photonics* **7**(1), 1–65 (2015).
30. K. K. Chan and S. Tang, "High-speed spectral domain optical coherence tomography using non-uniform fast Fourier transform," *Biomedical Optics Express* **1**(5), 1309–1319 (2010).
31. Z. Hu and A. M. Rollins, "Fourier domain optical coherence tomography with a linear-in-wavenumber spectrometer," *Optics Letters* **32**(24), 3525–3527 (2007).
32. R. Leitgeb, W. Drexler, A. Unterhuber, B. Hermann, T. Bajraszewski, T. Le, A. Stingl and A. Fercher, "Ultrahigh resolution Fourier domain optical coherence tomography," *Optics Express* **12**(10), 2156–2165 (2004).
33. T. Bajraszewski, M. Wojtkowski, M. Szkulmowski, A. Szkulmowska, R. Huber and A. Kowalczyk, "Improved spectral optical coherence tomography using optical frequency comb," *Optics Express* **16**(6), 4163–4176 (2008).
34. C. B. Scruby and L. E. Drain, *Laser Ultrasonics: Techniques and Applications* (Adam Hilger, Bristol, England, 1990), pp. 85–89.
35. M. Szkulmowski, S. Tamborski and M. Wojtkowski, "Spectrometer calibration for spectroscopic Fourier domain optical coherence tomography," *Biomedical Optics Express* **7**(12), 5042–5054 (2016).
36. Y. Yasuno, V. D. Madjarova, S. Makita, M. Akiba, A. Morosawa, C. Chong, T. Sakai, K.-P. Chan, M. Itoh and T. Yatagai, "Three-dimensional and high-speed swept-source optical coherence tomography for in vivo investigation of human anterior eye segments," *Optics Express* **13**(26), 10652–10664 (2005).

37. Micron Optics Inc., "FFP-TF2 Fiber Fabry-Perot Tunable Filter Technical Reference," <http://www.micronoptics.com/wp-content/uploads/2016/08/Fiber-Fabry-Perot-Tunable-Filter-Technical-Reference.pdf> (Accessed 7 February 2018).
38. BIPM, IEC, IFCC, ILAC, ISO, IUPAC, IUPAP and OIML, *International vocabulary of metrology – Basic and general concepts and associated terms* (JCGM, 2008).
39. A. Winarno, S. Takahashi, A. Hirai, K. Takamasu and H. Matsumoto, "Absolute measurement of gauge block without wringing using tandem low-coherence interferometry," *Measurement Science and Technology* **23**(12), 125001 (2012).
40. Y. Zhao, G. Schmidt, D. T. Moore and J. D. Ellis, "Absolute thickness metrology with submicrometer accuracy using a low-coherence distance measuring interferometer," *Applied Optics* **54**(25), 7693–7700 (2015).
41. E. N. Morel, N. A. Russo, J. R. Torga and R. Duchowicz, "Interferometric system based on swept source-optical coherence tomography scheme applied to the measurement of distances of industrial interest," *Optical Engineering* **55**(1), 014105 (2016).
42. P. Herrmann, "Determination of thickness, refractive index, and dispersion of waveguiding thin films with an Abbe refractometer," *Applied Optics* **19**(19), 3261–3262 (1980).
43. I. D. Nikolov and C. D. Ivanov, "Optical plastic refractive measurements in the visible and the near-infrared regions," *Applied Optics* **39**(13), 2067–2070 (2000).
44. E. Garcia-Caurel, A. De Martino, J.-P. Gaston and L. Yan, "Application of spectroscopic ellipsometry and Mueller ellipsometry to optical characterization," *Applied Spectroscopy* **67**(1), 1–21 (2013).
45. K. Peterlinz and R. Georgiadis, "Two-color approach for determination of thickness and dielectric constant of thin films using surface plasmon resonance spectroscopy," *Optics Communications* **130**(4-6), 260–266 (1996).
46. M. Haruna, M. Ohmi, T. Mitsuyama, H. Tajiri, H. Maruyama and M. Hashimoto, "Simultaneous measurement of the phase and group indices and the thickness of transparent plates by low-coherence interferometry," *Optics Letters* **23**(12), 966–968 (1998).
47. J. Yao, J. Huang, P. Meemon, M. Ponting and J. P. Rolland, "Simultaneous estimation of thickness and refractive index of layered gradient refractive index optics using a hybrid confocal-scan swept-source optical coherence tomography system," *Optics Express* **23**(23), 30149–30164 (2015).
48. J. Park, J. Bae, J. Jin, J.-A. Kim and J. W. Kim, "Vibration-insensitive measurements of the thickness profile of large glass panels," *Optics Express* **23**(26), 32941–32949 (2015).

49. K. Birch and M. Downs, "Correction to the updated Edlén equation for the refractive index of air," *Metrologia* **31**(4), 315–316 (1994).
50. A. L. Buck, "New equations for computing vapor pressure and enhancement factor," *Journal of Applied Meteorology* **20**(12), 1527–1532 (1981).
51. P. E. Ciddor, "Refractive index of air: new equations for the visible and near infrared," *Applied Optics* **35**(9), 1566–1573 (1996).
52. V. Korpelainen, J. Seppä and A. Lassila, "Measurement strategies and uncertainty estimations for pitch and step height calibrations by metrological atomic force microscope," *Journal of Micro/Nanolithography, MEMS, and MOEMS* **11**(1), 011002 (2012).
53. E. Diaz and M. Knobl, "Prototyping illumination systems with stock optical components," in *Photonik* 3/2012.
54. W. D. Callister and D. G. Rethwisch, *Fundamentals of Materials Science and Engineering*, 3rd edn. (John Wiley & Sons, Asia, 2008), pp. 708–711.
55. D. W. Kammler, *A First Course in Fourier Analysis* (Cambridge University Press, New York, United States of America, 2007), pp. 138–140.
56. BIPM, IEC, IFCC, ILAC, ISO, IUPAC, IUPAP and OIML, *Evaluation of measurement data – Guide to the expression of uncertainty in measurement* (JCGM, 2008).
57. Copper Development Association Inc., "Properties of Wrought and Cast Copper Alloys," <https://www.copper.org/resources/properties/db/basic-search.php> (Accessed 9 February 2018).
58. T.-H. Tsai, C. Zhou, D. C. Adler and J. G. Fujimoto, "Frequency comb swept lasers," *Optics Express* **17**(23), 21257–21270 (2009).
59. G. Finet, E. Maurincomme, A. Tabib, R. J. Crowley, I. Magnin, R. Roriz, J. Beaune and M. Amiel, "Artifacts in intravascular ultrasound imaging: Analyses and implications," *Ultrasound in Medicine & Biology* **19**(7), 533–547 (1993).
60. B. J. Kimura, V. Bhargava, W. Palinski, R. J. Russo and A. N. DeMaria, "Distortion of intravascular ultrasound images because of nonuniform angular velocity of mechanical-type transducers," *American Heart Journal* **132**(2, Part 1), 328–336 (1996).
61. ISO 230-7:2015, "Test code for machine tools – Part 7: Geometric accuracy of axes of rotation" (2015).
62. ISO 10360-2:2009, "Geometrical product specifications (GPS) – Acceptance and reverification tests for coordinate measuring machines (CMM) – Part 2: CMMs used for measuring linear dimensions" (2009).